nature neuroscience

Article

https://doi.org/10.1038/s41593-026-02254-8

HSV-1 strain H129 co-opts neuronal synaptic transmission machinery for its transsynaptic spread

Received: 2 January 2025

Accepted: 3 March 2026

Published online: 14 April 2026

Check for updates

Hai-Bin Qin[1,2], Yue-Peng Zhou[3], Yang Wu[3], Tian-Xiang Ji[1,2], An-Na Du[1], Ding Gao[1], Jin-Yan Sun[1], Xin-Ze Jiang[1,2], Zhi-Yuan Xu[1,2], Zhi-Yu Liu[1,2], Todd C. Holmes[4], Feng Xiong[3] ✉, Xin Zhou[3] ✉, Wen-Bo Zeng[1] ✉, Xing Liu[5] ✉, Cong-Jian Zhao[6] ✉, Yunyun Han[7] ✉ & Min-Hua Luo[1,2,3] ✉

The H129 strain (H129) of neurotropic herpes simplex virus-1 (HSV-1) is the only known HSV-1 strain that spreads transneuronally in a predominantly anterograde direction, leading to wide use for anterograde tracing in neural circuit mapping. However, it remains unclear whether H129 spreads in a synapse-specific manner or what mechanisms underlie its transmission. Here a microfluidic culture system for primary mouse cortical neurons and several engineered tool viruses were used to visualize the synapse-specific transmission of H129. We show that H129 particles are packaged into 'virion vesicles' that exploit the molecular machinery of Ca^{2+}-dependent neurotransmitter release, including voltage-gated calcium channels, synaptotagmin-7 and the SNARE complex, to exit the presynaptic bouton. Subsequently, H129 enters the postsynaptic neuron through gD/nectin-1 and clathrin-mediated endocytosis at the perisynaptic site. These findings clearly illustrate the molecular mechanistic sequence of HSV-1 transsynaptic spread, advance our understanding of the viral infection in the nervous system and provide design principles for further optimizing H129-derived anterograde neural tracers.

The α-herpesvirus, herpes simplex virus-1 (HSV-1), is a common neurotropic pathogen that spreads transneuronally in both the central nervous system (CNS) and the peripheral nervous systems[1]. Its transneuronal spread in the CNS enables rapid infection throughout the brain and potentially leads to life-threatening herpetic encephalitis due to neuronal damage from infection and inflammation[2]. Additionally, HSV-1 infection can cause the accumulation of phosphorylated tau in neurons, thus increasing the risk of Alzheimer's disease (AD) and transneuronal spread to other brain regions that may further promote the AD pathological cascade[3]. HSV-1's ability to transmit along brain circuitry offers the advantage of being a self-amplifying tracer for neural circuit mapping[4]. Despite its widespread use as a viral tracer by neuroscientists, there has been considerable debate about whether viral spread among neurons is synapse-specific, particularly regarding nonsynaptic release and its impact on the interpretation of circuit maps. Consequently, understanding the detailed mechanisms of HSV-1 transsynaptic spread is crucial for enhancing our ability to manage these infections and to study the connectome of the nervous system.

Increasing evidence suggests that HSV-1 can be transported anterogradely along the axon in a kinesin motor-assisted manner[5–7]. It is suspected that HSV-1 shares similar mechanisms with kinesin motor-assisted dense core vesicles (DCVs) transport, thus preferentially moving directionally toward axon terminals[8,9]. Transmission electron microscopy (TEM) imaging studies suggest that varicosities and growth cones may serve as sites for the envelopment of HSV-1 particles, with virions exiting through exocytosis[10], which may be similar to

A full list of affiliations appears at the end of the paper. ✉e-mail: xiongfeng@apm.ac.cn; xinzhou@wipm.ac.cn; zengwb@wh.iov.cn; xingliu1@szu.edu.cn; zhaocongjian@cqupt.edu.cn; yhan@hust.edu.cn; luomh@wh.iov.cn

DCVs' secretion. Thus, understanding the assembly and exit processes of HSV-1 is crucial for determining how it egresses from axons, especially at terminals. Recent studies indicate that the actin cytoskeleton in growth cones is essential for efficient HSV-1 exit from axons[11]. Another neurotropic herpesvirus, pseudorabies virus, is suggested to egress from axons independently of neuronal activity[12]. Despite these insights, little is known about the axonal exit process of HSV-1. There remains a gap in our understanding of whether HSV-1 specifically uses the molecular machinery of synaptic junctions or spreads more broadly in a nonspecific fashion. This lack of mechanistic clarity extends to many other neurotropic viruses, including measles virus, yellow fever virus, West Nile virus, vesicular stomatitis virus and rabies virus. All these viruses are known to transneuronally spread along neuronal circuits but lack definitive explanations for their transmission mechanisms[9,13].

Although the mechanisms of viral transsynaptic transmission are not well understood, there are tantalizing clues on how these process steps work. HSV-1 infection can induce spontaneous Ca^{2+} influx, with HSV-1 exiting axon terminals through exocytosis[10,14]. Interestingly, the SNARE protein VAMP2 and neuropeptide Y have been observed to cotransport with HSV-1 in the axon, suggesting that HSV-1 may use a synaptic vesicle secretory pathway for its transport[15]. However, it remains unknown whether the Ca^{2+}-dependent synaptic exocytosis machinery is involved in HSV-1's presynaptic exit. Furthermore, after exiting from the presynaptic neuron, how the virus enters postsynaptic neurons remains unclear.

HSV-1 strain H129 (H129) is a clinical isolate obtained from a human patient with herpetic encephalitis in 1977 (ref. 16). It exhibits similar features of infection, reproduction and anterograde spread in neurons among various species, including humans, cebus monkeys, tree shrew and mice[7,16–18]. It is the only known strain that preferentially spreads transneuronally in the anterograde direction[18]. In this study, we demonstrate that H129 is transmitted transsynaptically in a synapse-specific manner by co-opting the molecular machinery of Ca^{2+}-dependent presynaptic secretion and clathrin-mediated postsynaptic endocytosis. These findings will support future efforts to manage and control neurotropic viral infections and will be useful for developing better H129-derived neural tracers for precise and accurate neural circuit mapping.

Results

H129 transsynaptically transmits at the synapse of primary cortical neurons

Although H129 spreads transneuronally, potentially by transsynaptic transmission between efferent and afferent neurons[19], the mechanism of its transsynaptic infection remains unclear due to the difficulty in tracking transneuronal infection when presynaptic and postsynaptic neurons are intermixed in vivo and in vitro culture systems. To overcome this challenge, we developed a microfluidic system that consists of two chambers connected by microgrooves with a length of 700 µm, a width of 10 µm and a depth of 3 µm. Primary cultured cortical neurons plated in one chamber can only form synapses with neurons in the other chamber by extending their axons through the microgrooves[17,20]. We further optimized the microfluidic system for in vitro neuron culture to ensure that the synapses among neurons from the two chambers were concentrated near the microgrooves of the postsynaptic chamber, where the synaptic density and electrophysiological properties stabilize at 21 days in vitro (DIV21; Extended Data Fig. 1). Second, we determined that the hydrostatic pressure generated from the height difference between the two chambers enforced flow direction in the microgrooves to prevent the diffusion or leakage of the virus from directly infecting neurons in the opposite chamber (Extended Data Fig. 2a–c). Therefore, the initial infection was limited to the presynaptic chamber, allowing clear visualization of H129 transsynaptic transmission within the postsynaptic chamber near the microgrooves. The H129 progeny viral particles were readily observed in the postsynaptic chamber starting at 16 h postinfection (16 hpi; Extended Data Fig. 2d–f). Neurons in the presynaptic chamber were infected with H129-VP26-mCherry to visualize viral infection and spreading[7], the microfluidic chamber was removed at 24 hpi and both sides of the cultured neurons (with intact neurites) were fixed and stained with syntaxin-1 (STX-1) and postsynaptic-density protein 95 (PSD95), revealing notable colocalization of H129 particles (indicated by VP26-mCherry) with STX-1 and PSD95 (Fig. 1a–d). For other experiments to monitor H129 transsynaptic transmission, we constructed H129-VP26-mCherry-syBFP, a recombinant virus that simultaneously labeled presynaptic boutons with BFP-tagged synaptophysin, and revealed the location of viral particles; neurons in the postsynaptic chamber were transfected with pCMV-PSD95-eGFP to label the postsynaptic density (Fig. 1e,f). Between 16 and 24 hpi, the transsynaptic migration of H129 particles was tracked by live-cell imaging with a frequency of 0.1667 ± 0.0167 events per min per synapse (Fig. 1g–j). Remarkably, H129 transsynaptic transmission can be captured directly by TEM, showing the H129 virions situated within a double omega structure formed by presynaptic and postsynaptic membranes, accounting for 2.68% viral particles appearing in the area of the synapse (Fig. 1k,l). It suggests that the H129 virion may be secreted from the presynaptic bouton and subsequently enter the postsynaptic compartment.

Presynaptic assembly of H129 'virion vesicle' is required for its transsynaptic transmission

TEM images revealed a substantial number of viral particles in the presynaptic terminals, with viral capsids exhibiting structural similarities to DCVs, yet displaying distinct morphological features that served well for identification (Extended Data Fig. 3). As demonstrated, H129 was primarily transported in the form of capsids within the axon[7]. In the presynaptic boutons, we observed four types of viral particles, namely capsids, virions, 'virion vesicles' and secreting virions, with capsids constituting the largest proportion (Fig. 2a,b), suggesting that the H129

Fig. 1 | H129 transsynaptic transmission. a, Three-dimensional structure of microfluidic chamber and schematic diagram of neuron infection. Microfluidic chambers with presynaptic (pre) and postsynaptic (post) compartments connected by microgrooves allow synapse formation near the grooves (middle) at the post side. At DIV21, presynaptic neurons were infected with H129-VP26-mCherry (MOI = 1). A 100-µl medium volume difference maintained hydrostatic pressure to restrict initial infection to the precompartment (right). **b**–**d**, Colocalization of VP26-mCherry (presents viral particle), STX-1 (presynaptic marker) and PSD95 (postsynaptic marker). **b**, Confocal images show the colocalization (white arrowheads) of VP26-mCherry (red), STX-1 (blue) and PSD95 (green). The white dashed-rectangle boxed area was zoomed in (bottom), and the line profiles were further analyzed. **c**, Normalized line profiles of the intensity of VP26-mCherry, STX-1 and PSD95. **d**, Colocalization rate of VP26-mCherry with STX-1 and PSD95. Data are represented as mean ± s.e.m. **e**, Schematic genome diagram of engineered H129-VP26-mCherry-syBFP virus (left) and pCMV-PSD95-eGFP construct (right). **f**–**j**, Live imaging of H129 transsynaptic transmission. **f**, Postsynaptic neurons were transfected with pCMV-PSD95-eGFP at DIV7, and presynaptic neurons infected with H129-VP26-mCherry-syBFP at DIV21. **g**, Live imaging of H129 transsynaptic transmission. BF, VP26-mCherry (red), syBFP (blue), PSD95-eGFP (green) and colocalization (white arrowhead) are shown. **h**, Snapshots of an H129 transsynaptic transmission event and the white dashed-line circle indicated the ROI for movement analysis. **i**, dF/F_0 traces of H129 transsynaptic transmission event over time. **j**, Frequency of H129 transsynaptic transmission events (transsynaptic events per min per synapse). Data are represented as mean ± s.e.m. **k**,**l**, H129 transsynaptic transmission. **k**, TEM images. The H129 particle crosses the synapse, where the presynaptic and postsynaptic membranes show a double Ω structure. **l**, The percentage of H129 particles in presynaptic bouton, perisynaptic cleft and postsynaptic compartments, respectively. BF, brightfield; ROI, region of interest; BAC, bacterial artificial chromosome; *F*, fluorescence intensity.

https://doi.org/10.1038/s41593-026-02254-8

capsid might be assembled into a 'virion vesicle' at the presynaptic bouton for secretion. Notably, TEM images showed morphologically different stages of H129 capsid engulfment by autophagy-like membranes, ultimately forming 'virion vesicles' within the presynaptic boutons (Fig. 2c). Viruses, including herpesviruses, are capable of adopting secretory autophagy for their assembly and egress[21]. To examine whether H129 particles are engaged with autophagic flux, neurons in the presynaptic chamber were infected with H129-VP26-mCherry, further fixed and stained with STX-1 and LC3b at 24 hpi. A substantial portion of H129 particles colocalized with LC3b at presynaptic boutons (Extended Data Fig. 4a–d). Additionally, live imaging with H129-VP26-mCherry-sybFP-P2A-eGFP-LC3b, expressing with BFP-tagged synaptophysin and eGFP-tagged LC3b to enable the visualization of the relative location of viral particles with presynaptic boutons and autophagosomes (Extended Data Fig. 4e), showed that LC3b colocalizes with, and cotransports with, H129 particles at presynaptic boutons. A similar fraction of colocalized H129 particles with LC3b at presynaptic boutons was also observed by immunofluorescence assay (IFA; Extended Data Fig. 4f–h). We further tested with a previously developed dual-labeled virus, H129-VP26-mCherry-gD-eGFP, in which the capsid was labeled with VP26-mCherry and the envelope with gD-eGFP (C terminal of glycoprotein D fused with eGFP[7]; Extended Data Fig. 4i), showing that ~90% enveloped viral particles (VP26-mCherry$^+$ and gD-eGFP$^+$) were also LC3b-positive (Extended Data Fig. 4j–l). These

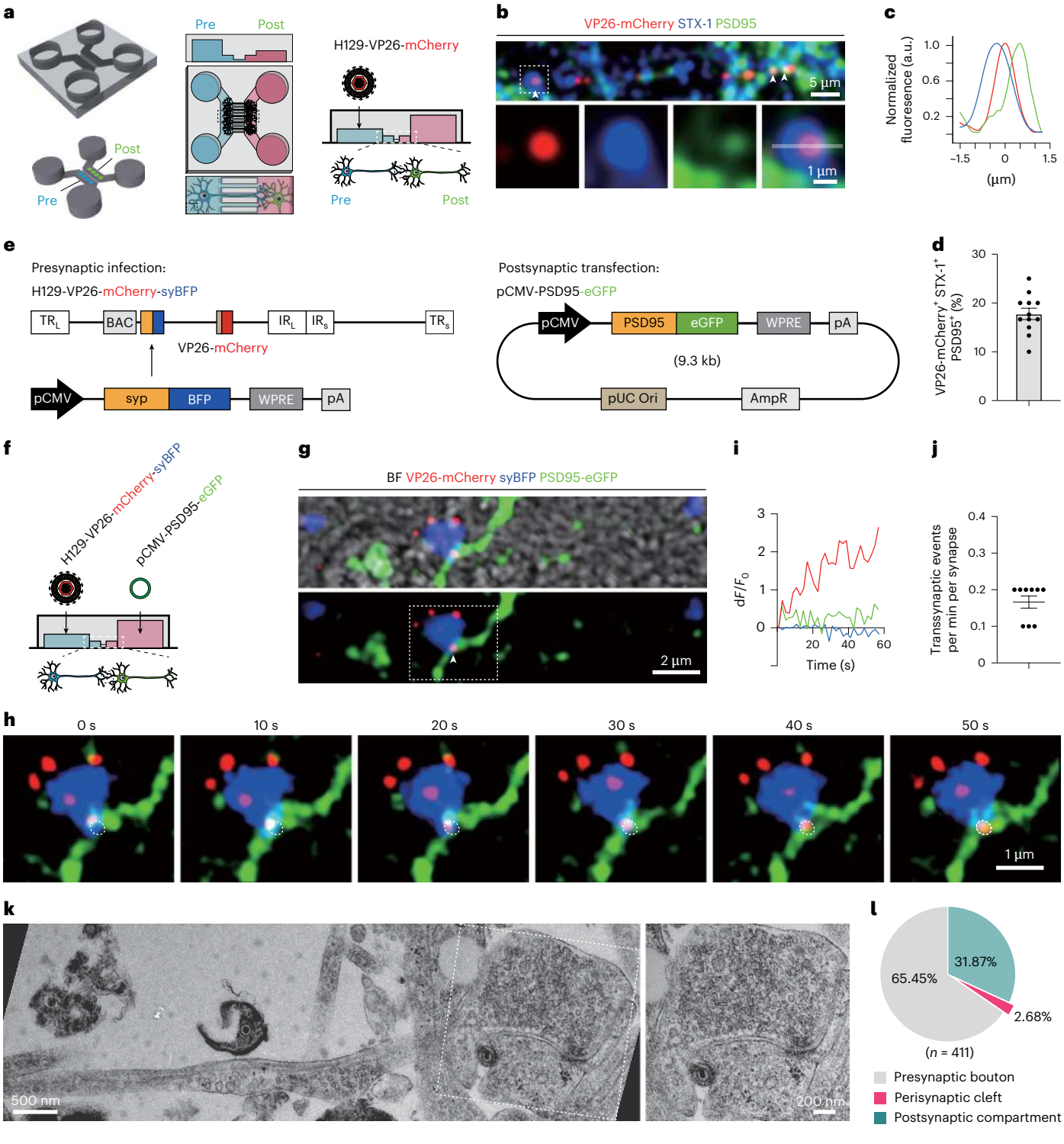

results indicate that autophagic flux may contribute to the assembly and secretion of H129.

To verify the contribution of autophagic flux to 'virion vesicle' assembly, 3-methyladenine (3-MA), the classical autophagy inhibitor, was applied to the presynaptic boutons after infection with H129-VP26-mCherry at 16 hpi. Light microscopy and TEM analysis at 24 hpi (Fig. 2d) showed that transsynaptic H129 infection is significantly impeded by 3-MA in a dose-dependent manner, as the number of infected neurons in the postsynaptic chamber decreases (Fig. 2e,g). Correspondingly, 3-MA treatment caused H129 particle arrest in presynaptic boutons as shown by a marked increase in the colocalization of VP26-mCherry with STX-1 and an increase in the size of VP26-mCherry puncta at the presynaptic boutons (Fig. 2f,h). TEM images confirmed that the formation of 'virion vesicle' was inhibited by 3-MA treatment, with the proportion of 'virion vesicles' decreasing from 7% to 3% and secreting virions decreasing from 25% to 5%, indicating a crucial role of assembly of 'virion vesicles' in viral secretion (Fig. 2i,j). The total number of H129 particles and the number of capsids in presynaptic boutons significantly increased with 3-MA treatment (Fig. 2j,k). Similarly, after infection with H129-VP26-mCherry-gD-eGFP and treatment with 3-MA, the proportion of enveloped viral particles dramatically decreased from ~30% to ~9%, consistent with the TEM data (~34% to ~10%, including virion, 'virion vesicle' and secreting virion; Extended Data Fig. 4m–o and Fig. 2j). These findings suggest that the presynaptic encapsulation of H129 particles into 'virion vesicles' is an essential preceding step for presynaptic secretion and subsequent transsynaptic transmission.

Membrane depolarization facilitates presynaptic secretion of H129

To investigate H129 presynaptic secretion, we constructed H129-VP26-mCherry-pHluorin-gD. Superecliptic pHluorin fused to the N terminal of gD exposed on the virion surface[22] (Fig. 3a) remains quenched within the 'virion vesicle', as secretory vesicles typically maintain an acidic pH range of 4.5–5.5 (refs. 23,24), but the bright pHluorin-gD fluorescence burst can be observed upon the 'virion vesicle' fusing with the plasma membrane and being released into the extracellular space (Fig. 3a and Extended Data Fig. 5a–d), which can be used to observe and quantify the presynaptic secretion of H129 particles with live imaging (Fig. 3b–d).

TEM directly captured 'virion vesicle' secretion, showing stages from initial attachment at the presynaptic membrane to the complete collapse (Fig. 3e). To characterize this process, we measured two parameters—the pore membrane angle (θ; Fig. 3e, marked in red) at the junction of the plasma and vesicular membranes, and the secretion cavity depth (d; Fig. 3e, marked in purple), defined as the tangent length from the fusion pore to the vesicular membranes[25,26]. Multipeak Gaussian fitting of these parameters reveals a three-peak distribution (Fig. 3f,g), suggesting a sequential three-stage release process. Initially, the 'virion vesicle' rapidly attached to the plasma membrane, displaying small pore angles and long cavity distances, followed by an intermediate slower secretion phase, and a final stable full secretion stage, characterized by large pore angles and very short cavity depths (Fig. 3h). This process resembles the rapid fusion of neurotransmitter vesicles[27], indicating that H129 virions use similar presynaptic machinery for exit.

To determine whether H129 secretion is activity dependent, like neurotransmitter release, tetrodotoxin (TTX) or KCl was applied separately to the presynaptic boutons at 16 hpi after H129-VP26-mCherry infection. Samples were then collected for analysis at 24 hpi (Extended Data Fig. 5e). While TTX treatment had no noticeable effect (Extended Data Fig. 5f,g), KCl significantly enhanced transsynaptic spread of H129 (Extended Data Fig. 5h,i). Virion secretion events, 150s after the KCl perfusion, were observed by imaging as a rapid increase in pHluorin fluorescence, with presynaptic neurons that were infected with H129-VP26-mCherry-pHluorin-gD (Fig. 3i,j). The frequency of pHluorin-indicated H129 virion secretion events increased at least twofold in the presence of KCl (Fig. 3k). TEM analysis further confirmed that KCl-induced depolarization nearly depleted 'virion vesicles' within the presynaptic boutons, doubling the number of virions undergoing fusion at the plasma membrane (Fig. 3l–n). Collectively, H129 'virion vesicles' exit occurs through rapid membrane fusion, a process evoked by depolarization and sharing mechanistic features with neurotransmitter release.

Ca^{2+} influx is required for presynaptic secretion of H129

To investigate whether and how the secretion of H129 virions depends on presynaptic secretion and Ca^{2+} influx like neurotransmitter release, we constructed the recombinant virus H129-VP26-mCherry-syGCaMP3.5 to monitor the presynaptic Ca^{2+} dynamics of the infected presynaptic neurons (Fig. 4a). Spontaneous Ca^{2+} influx, with a frequency of 1.435 ± 0.179 events per min per bouton, was observed in the presynaptic boutons where H129 particles are located (Fig. 4b,c and Extended Data Fig. 6a), consistent with the previous observed herpesvirus infection induces Ca^{2+} influx in neuronal soma[28].

The necessity of Ca^{2+} influx for virion release was tested with Ca^{2+} chelators. Depleting extracellular Ca^{2+} with EGTA blocked H129 transsynaptic transmission (Extended Data Fig. 6b–d) and caused H129 particles to accumulate at presynaptic boutons, evidenced by increased H129/STX-1 colocalization and enlarged H129 puncta (Fig. 4d,e). TEM confirmed that EGTA nearly eliminated virion secretion, leading to an accumulation of retained 'virion vesicles' (Fig. 4f–h and Extended Data Fig. 6e). This indicates that extracellular Ca^{2+} is crucial for the release of 'virion vesicles'. Similarly, buffering Ca^{2+} influx through the Ca^{2+} channels during action potentials (APs) with BAPTA-AM blocked H129 transsynaptic transmission (Extended Data Fig. 6f,g) and resulted in the presynaptic accumulation of H129 'virion vesicles', significantly reducing the number of secreting virions in the synaptic cleft (Fig. 4i–m and Extended Data Fig. 6h). These findings suggest that Ca^{2+} influx into the presynaptic boutons is necessary for H129 'virion vesicle' secretion.

Next, we investigated the potential calcium channels involved in H129 presynaptic secretion, by applying selective

Fig. 2 | Assembly of H129 'virion vesicle' is required for its transsynaptic transmission. a,**b**, The forms of H129 particles, capsid, virion, 'virion vesicle' and secreting virion in presynaptic boutons. **a**, TEM images of the different types of H129 particles at presynaptic bouton. **b**, The percentage of different H129 particles. **c**, TEM images of different stages of H129 capsid assembly into 'virion vesicle' at presynaptic bouton. **d**–**k**, Effect of 3-MA on H129 'virion vesicle' presynaptic assembly and transsynaptic transmission. **d**, Diagram of infection presynaptic neurons (left), timeline of virus infection and 3-MA treatment (right). **e**, Confocal images of H129-VP26-mCherry transneuronal spread (DAPI, blue; VP26-mCherry, red) after 3-MA treatment (0 μM (control), 5 μM and 10 μM). Solid lines mark microgroove borders; dashed rectangle shows VP26-mCherry signal only (right). **f**, Confocal images show colocalization (white arrowheads) of VP26-mCherry, STX-1 and PSD95 after 3-MA treatment. **g**, Normalized number of postsynaptic infected neurons after 3-MA treatment. Data were analyzed by one-way ANOVA, Tukey test. **h**, The colocalization analysis of VP26-mCherry with STX-1 (top) and normalized VP26-mCherry puncta size at presynaptic bouton after 3-MA treatment (bottom). Data were analyzed by one-way ANOVA, Tukey test. **i**, TEM images of H129 particles in presynaptic boutons without or with 10 μM 3-MA treatment ('virion vesicle', green arrowhead; capsid, black arrowheads). **j**, The percentage of viral particles in presynaptic bouton. **k**, Count H129 particles per presynaptic bouton. Total H129 particles per presynaptic bouton (n = 92 and n = 40 viral particle containing boutons for control and 3-MA treatment groups, top). H129 capsids per presynaptic bouton (n = 61 and n = 40 capsid containing boutons for control and 3-MA treatment groups, bottom). Data were analyzed by two-tailed unpaired t test. Data are represented as mean ± s.e.m., $^{**}P < 0.01$ and $^{****}P < 0.0001$.

https://doi.org/10.1038/s41593-026-02254-8

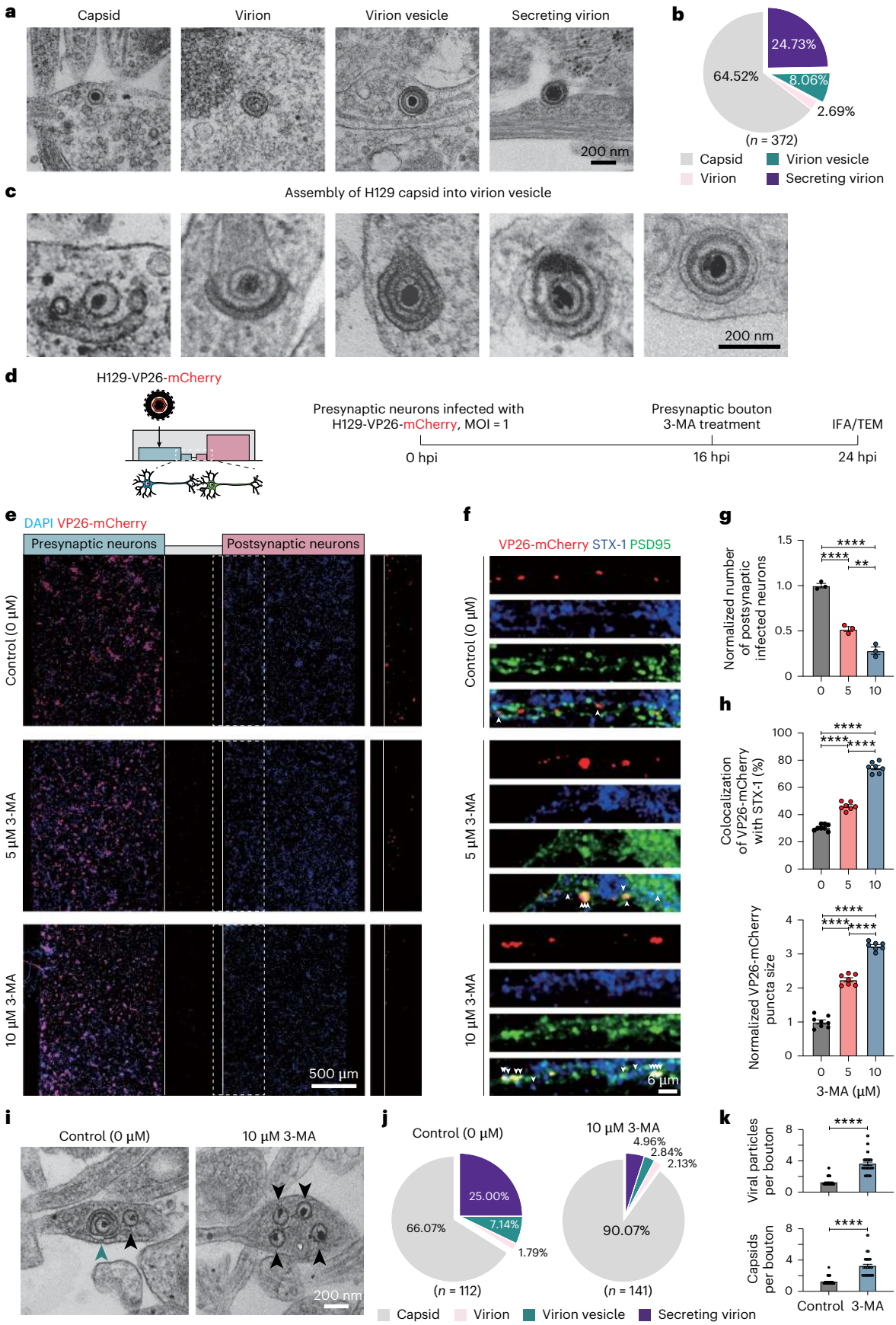

https://doi.org/10.1038/s41593-026-02254-8

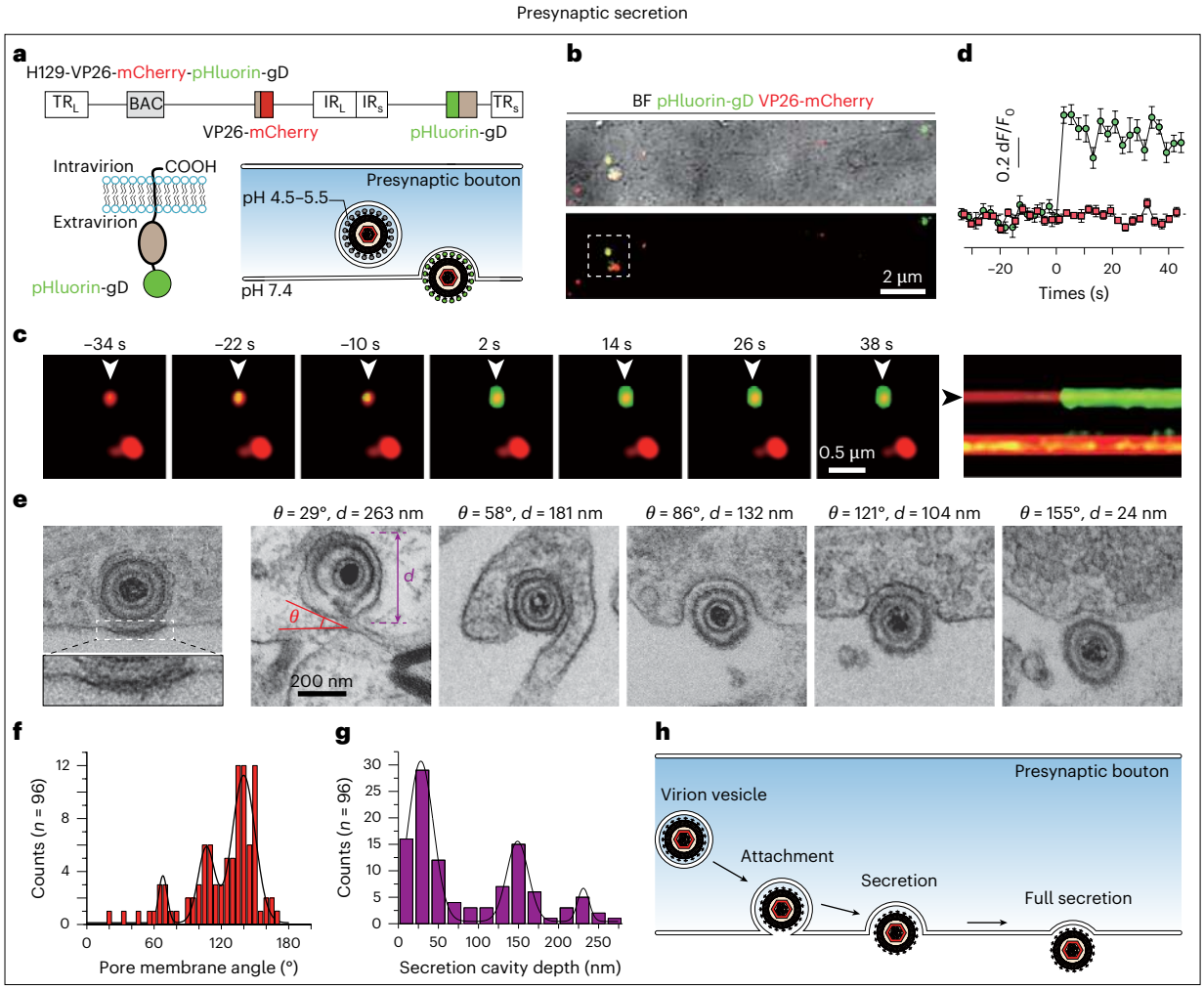

https://doi.org/10.1038/s41593-026-02254-8

Fig. 3 | H129 'virion vesicles' are released by presynaptic secretion upon depolarization. a, Schematic illustration of H129-VP26-mCherry-pHluorin-gD. **b**–**d**, Live imaging of presynaptic secretion of H129-VP26-mCherry-pHluorin-gD. **b**,**c**, A presynaptic secretion event of H129-VP26-mCherry-pHluorin-gD (**b**), expansion of the region indicated by dashed box (**c**, left) and the corresponding kymograph (**c**, right). **d**, Averaged fluorescence trace from 12 secretion events. **e**–**h**, TEM imaging of H129 'virion vesicle' presynaptic secretion. **e**, H129 'virion vesicle' attaching to the presynaptic membrane (left, with zoomed inset below) and subsequent secretion stages (right). Pore membrane angle (θ, red) and secretion cavity depth (d, purple) quantify secretion, with values shown above images. Histograms of pore angle (**f**) and cavity depth (**g**) during H129 presynaptic secretion, analyzed by Gaussian distribution. **h**, Schematic model of H129 presynaptic secretion—similar ratios of pore angle and cavity depth correspond to attachment (~10%; 50–90°, 200–275 nm), secretion (~30%; 90–120°, 100–200 nm) and full secretion (~60%; 120–180°, 0–100 nm). **i**–**k**, H129 presynaptic secretion and KCl stimulation by live imaging. **i**, Live imaging of H129-VP26-mCherry-pHluorin-gD presynaptic secretion (appearance of pHluorin-gD, white arrowheads) responding to KCl stimulation. **j**, Averaged response of pHluorin-gD and VP26-mCherry. **k**, Frequency of H129 secretion events in presynaptic boutons (events per min per 1,000 μm^2, two-tailed unpaired t test). **l**–**n**, H129 presynaptic secretion and KCl stimulation by TEM. **l**, TEM images of H129 presynaptic secretion without or with KCl stimulation ('virion vesicle', green arrowhead; secreting virion, purple arrowheads). **m**, The percentage of different viral particles in presynaptic boutons. **n**, Counts of secreting virions per presynaptic bouton ($n = 25$ and $n = 22$ secreting virion containing boutons for control and KCl stimulation groups, respectively; two-tailed Mann–Whitney U test). Data are represented as mean ± s.e.m., $^{**}P < 0.01$ and $^{****}P < 0.0001$.

blockers for N-type[29], P/Q-type[30], R-type[31], T-type[32] and L-type channels[33] (Extended Data Fig. 6b). Only SNX-482 (250 nM), an R-type channel blocker, significantly reduces the number of infected postsynaptic neurons (Extended Data Fig. 6i,j). After SNX-482 treatment, H129 particles accumulated at presynaptic boutons, evidenced by increased colocalization of viral particles with STX-1 and enlarged VP26-mCherry puncta at presynaptic boutons (Fig. 4n–o). TEM analysis confirmed 'virion vesicles' accumulation in the presynaptic boutons, showing a twofold to threefold increase in both the number and proportion of 'virion vesicles' within the boutons (Fig. 4p–r and Extended Data Fig. 6k). These findings suggest that Ca^{2+} influx through R-type calcium channel has an important role in H129 presynaptic secretion.

Syt7 and SNARE complex mediate the release of H129 'virion vesicles' from presynaptic boutons

To test whether H129 co-opts the synaptic transmission machinery to exit neurons, we investigated the role of calcium sensors and SNARE proteins in virion secretion. We knocked down the expression of synaptotagmin-1 (Syt1) and synaptotagmin-7 (Syt7) using recombinant viruses of H129-VP26-mCherry-Syt1^{sh} and H129-VP26-mCherry-Syt7^{sh} that expressed the targeting shRNA alongside viral replication, respectively (Fig. 5 and Extended Data Figs. 7 and 8). The knockdown vectors effectively reduce Syt1 and Syt7 expression by over 50% (Extended Data Figs. 7a,b and 8a,b). While Syt1 knockdown had no effect (Extended Data Fig. 7c–e), Syt7 knockdown significantly inhibited H129 transsynaptic spread (Extended Data Fig. 8c–e), leading to presynaptic accumulation of H129 particles, as shown by increased colocalization of viral particles with STX-1 and larger H129 puncta at presynaptic sites (Fig. 5a–c). TEM images further confirmed an increase of 'virion vesicles' within the presynaptic boutons of Syt7 KD neurons (Fig. 5d–f and Extended Data Fig. 8f). This deficit was rescued by the vector coexpressing shRNA with a rescue gene Syt7 (Syt7^{WT}) but not by coexpressing a mutant (Syt7^{C2A*B*}) with impaired Ca^{2+} binding function (Fig. 5a). Syt7^{WT} successfully restores H129 transsynaptic transmission (Extended Data Fig. 8d,e) and reduces viral particle accumulation and H129 puncta size in the presynaptic boutons (Fig. 5b,c). In contrast, Syt7^{C2A*B*} fails to rescue the H129 transsynaptic transmission deficit caused by Syt7 knockdown, resulting in continued accumulation of 'virion vesicles' in the presynaptic boutons (Fig. 5d–f and Extended Data Fig. 8f). These findings suggest that Syt7 acts as a Ca^{2+} sensor for the presynaptic secretion of H129 'virion vesicles'.

To investigate whether the presynaptic secretion of H129 occurs through SNARE complex-mediated membrane fusion, we treated the infected neurons with TeNT, which cleaves VAMP[34,35] (Extended Data Fig. 9a). TeNT decreased the number of infected postsynaptic neurons significantly in a dose-dependent manner (Extended Data Fig. 9b,c), and caused presynaptic accumulation of H129 particles, indicated by increases both in colocalization of viral particles with STX-1 and VP26-mCherry puncta size (Fig. 5g,h and Extended Data Fig. 9d). TEM images further confirmed the accumulation of 'virion vesicles' caused by TeNT (Fig. 5i–k and Extended Data Fig. 9e). Similarly, shRNA-mediated knockdown of VAMP2 using H129-VP26-mCherry-VAMP2^{sh} inhibited H129 transsynaptic transmission (Extended Data Fig. 9f–j), and led to H129 accumulation in the presynaptic boutons, as shown by marked increases in colocalization of viral particles with STX-1 and VP26-mCherry puncta size (Fig. 5l–m and Extended Data Fig. 9k). TEM images confirmed the similar results (Fig. 5n–p and Extended Data Fig. 9l). Collectively, these findings show that H129 uses Syt7 and the SNARE complex for its presynaptic secretion, mirroring the molecular mechanism of neurotransmitter release.

gD and clathrin-mediated endocytosis are essential for H129 to enter postsynaptic neurons transsynaptically

We have determined the molecular mechanisms underlying presynaptic events that mediate H129 packaging and release from presynaptic neurons. Next, we aim to investigate how H129 enters the postsynaptic neuron. Although the gD domain of HSV-1 interacts with multiple receptors for entering host cells, including nectin-1, herpesvirus entry mediator (HVEM), and 3-O-sulfated heparan sulfate[36], only nectin-1 is located at the postsynaptic membrane and functions as a synaptic adhesion molecule, and also has a role in synapse formation[37]. Additionally,

Fig. 4 | H129 'virion vesicle' secretion depends on presynaptic Ca^{2+} influx through R-type channels. a, Genomic diagram of H129-VP26-mCherry-syGCaMP3.5. **b**,**c**, H129 infection and presynaptic Ca^{2+} influx. **b**, Live imaging of presynaptic H129 particles and spontaneous Ca^{2+} transient (syGCaMP3.5, green). **c**, Averaged fluorescence trace from 12 presynaptic Ca^{2+} events (top) and kymographs from the dashed-line boxed region in **b** (bottom). **d**–**h**, H129 presynaptic secretion and EGTA treatments. **d**, Confocal images show colocalization (white arrowhead) of VP26-mCherry, STX-1 and PSD95 after treatment with EGTA (control (0 mM), 5 mM and 10 mM). **e**, Analysis of VP26-mCherry colocalization with STX-1 and normalized VP26-mCherry puncta size at presynaptic boutons (one-way ANOVA, Tukey test). **f**, TEM image of accumulated H129 'virion vesicles' in presynaptic bouton after EGTA treatment (pseudocolor of light red merged with green). **g**, The percentage of different viral particles in presynaptic boutons. **h**, Counts of 'virion vesicles' per presynaptic bouton ($n = 12$ and $n = 22$ 'virion vesicle' containing boutons for control and EGTA treatment groups, respectively; two-tailed unpaired t test). **i**–**m**, H129 presynaptic secretion and BAPTA-AM treatment, similar to **d**–**h**. **m**, Counts of 'virion vesicles' per presynaptic bouton without or with BAPTA-AM treatment ($n = 13$ and $n = 24$ 'virion vesicle' containing boutons for control and BAPTA-AM treatment groups, respectively; two-tailed unpaired t test). **n**–**r**, H129 presynaptic secretion and treatment with SNX-482, similar to **d**–**h**. **r**, Counts of 'virion vesicles' per presynaptic bouton without or with SNX-482 treatment ($n = 9$ and $n = 22$ 'virion vesicle' containing boutons for control and SNX-482 treatment groups, respectively; two-tailed unpaired t test). Data are represented as mean ± s.e.m., $^{*}P < 0.05$, $^{***}P < 0.001$ and $^{****}P < 0.0001$.

https://doi.org/10.1038/s41593-026-02254-8

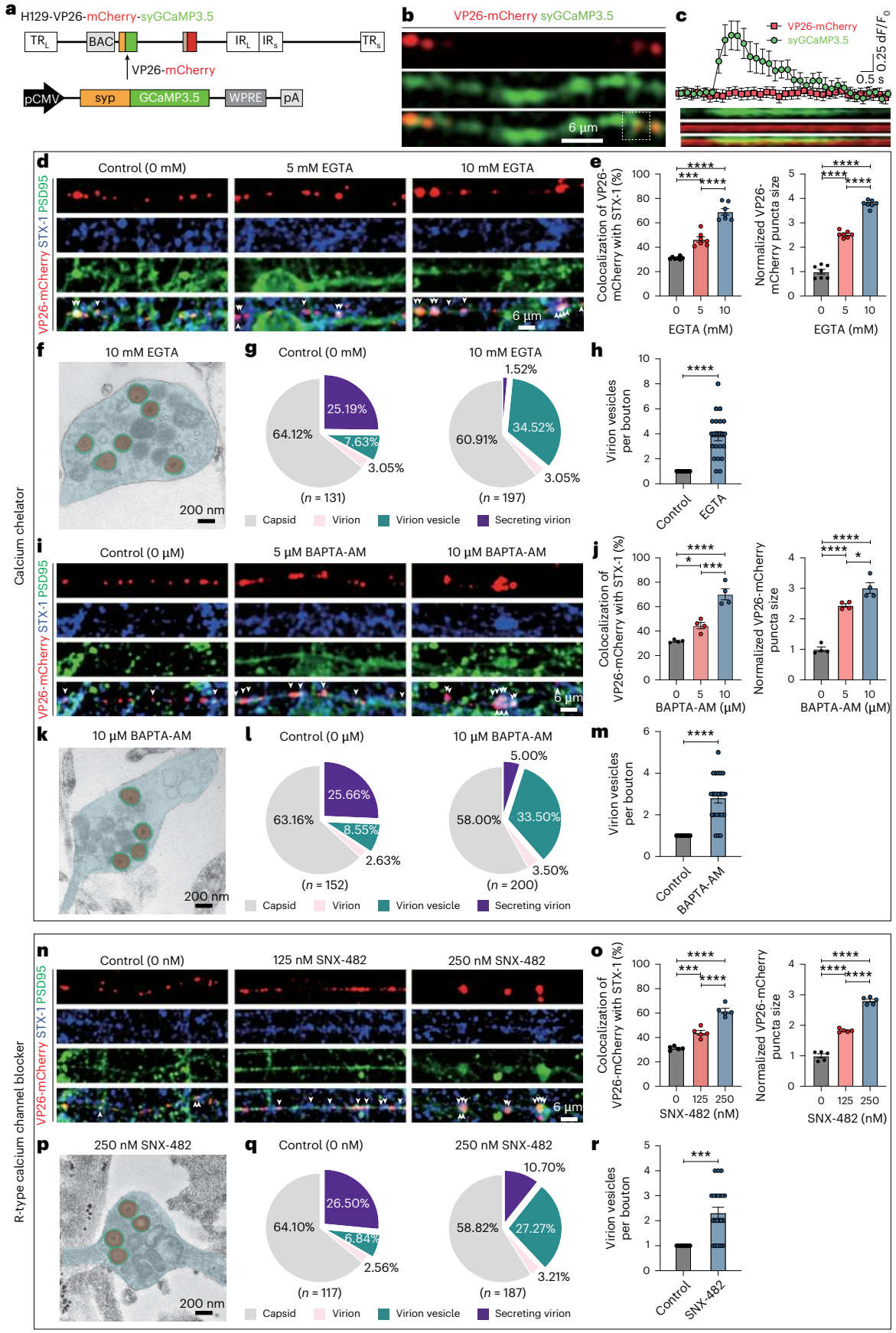

https://doi.org/10.1038/s41593-026-02254-8

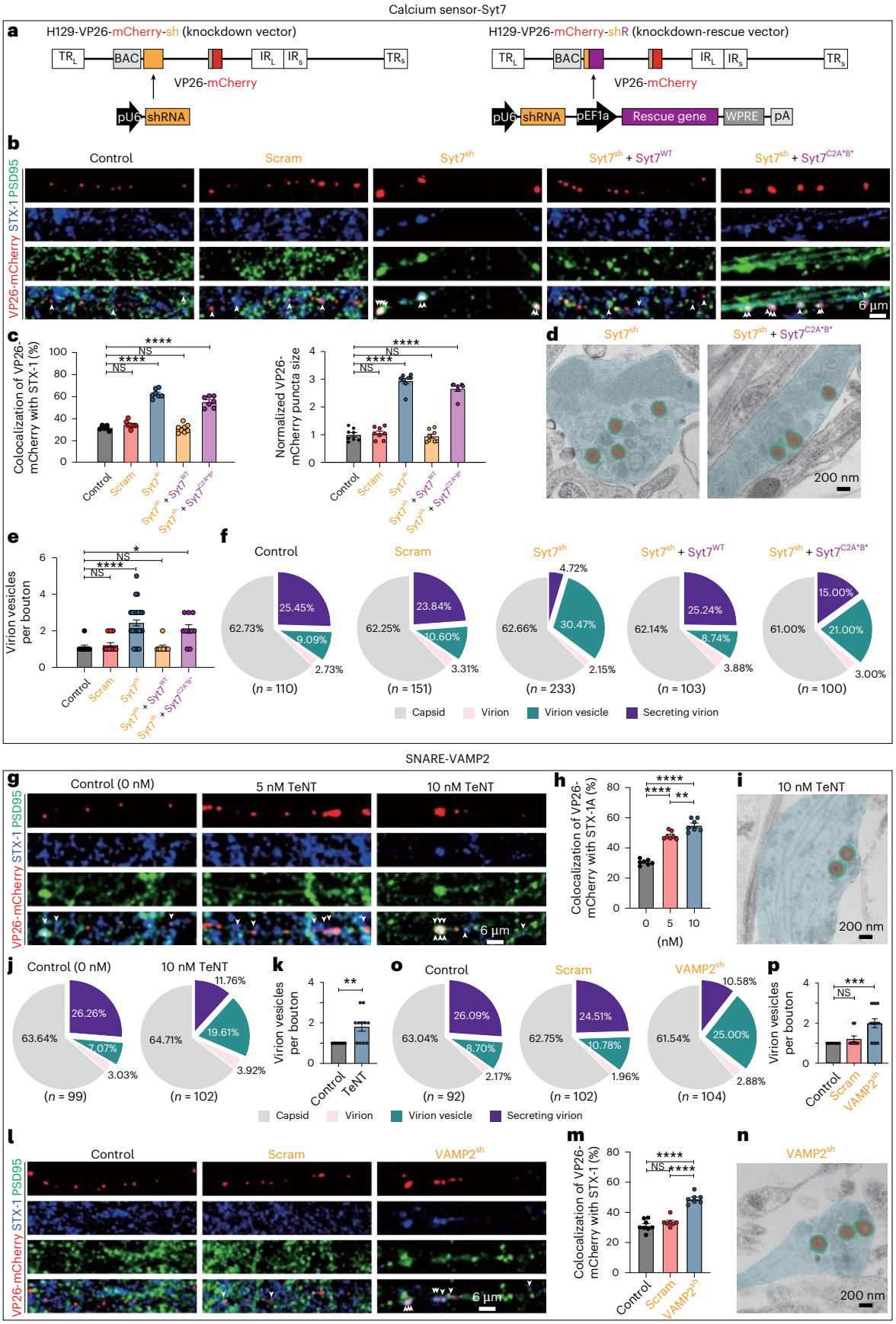

https://doi.org/10.1038/s41593-026-02254-8

Fig. 5 | H129 presynaptic secretion is mediated by Syt7 and SNARE complex. **a**, Genomic diagram of H129-VP26-mCherry-sh (knockdown vector, left) and H129-VP26-mCherry-shR (knockdown-rescue vector, right). **b**–**f**, H129 presynaptic secretion and calcium sensor Syt7. **b**, Confocal images show the colocalization (white arrowheads) of VP26-mCherry STX-1 and PSD95 after infection with H129-VP26-mCherry (control), H129-VP26-mCherry-Scram (scram), H129-VP26-mCherry-Syt7^{sh} (Syt7^{sh}), H129-VP26-mCherry-Syt7^{sh} + Syt7^{WT} (Syt7^{sh} + Syt7^{WT}) and H129-VP26-mCherry-Syt7^{sh} + Syt7^{C2A*B*} (Syt7^{sh} + Syt7^{C2A*B*}). **c**, Analysis of VP26-mCherry colocalization with STX-1 and normalized VP26-mCherry puncta size at presynaptic boutons after infection (one-way ANOVA, Tukey test). **d**, TEM images show 'virion vesicles' accumulation in presynaptic bouton after infection with Syt7^{sh} and Syt7^{sh} + Syt7^{C2A*B*} (pseudocolor of light red merged with green). **e**, Counts of 'virion vesicles' per presynaptic bouton after infection (n (control) = 9, n (scram) = 13, n (Syt7^{sh}) = 32, n (Syt7^{sh} + Syt7^{WT}) = 9, n (Syt7^{sh} + Syt7^{C2A*B*}) = 10 'virion vesicle' containing boutons, one-way ANOVA, Tukey test). **f**, The percentage of viral particles in presynaptic boutons after infections. **g**–**k**, H129 presynaptic secretion and SNARE-VAMP2 inhibitor, TeNT, similar to **b**–**f**. **k**, Counts of 'virion vesicles' per presynaptic bouton without or with TeNT treatment (n = 9 and n = 11 'virion vesicle' containing boutons for control and TeNT treatment groups, respectively; two-tailed unpaired t test). **l**–**p**, H129 presynaptic secretion and VAMP2 knockdown, similar to **b**–**f**. **p**, Counts of 'virion vesicles' per presynaptic bouton after infection (n (control) = 9, n (scram) = 9, n (VAMP2^{sh}) = 13 'virion vesicle' containing boutons, one-way ANOVA, Tukey test). Data are represented as mean ± s.e.m., $^{*}P < 0.05$, $^{**}P < 0.01$, $^{***}P < 0.001$ and $^{****}P < 0.0001$. NS, not significant.

it has been reported that nectin-1 can facilitate transcytosis to transfer cytoplasmic cargo, including infectious material, across cells[38].

IFA analysis revealed the colocalization of H129-VP26-mCherry particles with nectin-1 at synapses (Fig. 6a–c). To identify the specific interaction contributing to the re-entry, we used gD mutants—gD$^{d7\text{-}32}$ (blocks HVEM and 3-O-sulfated heparan sulfate binding, but not nectin-1)[39] and gD$^{Mut\ (D215G/R222N/F223I)}$ (specifically blocks viral nectin-1 binding, but not HVEM and 3-O-sulfated heparan sulfate)[40] to construct H129-VP26-mCherry-gD$^{d7\text{-}32}$ (gD$^{d7\text{-}32}$) and H129-VP26-mCherry-gD$^{Mut\ (D215G/R222N/F223I)}$ (gD$^{Mut\ (D215G/R222N/F223I)}$), respectively (Fig. 6d). Neurons in the presynaptic chamber were infected with H129-VP26-mCherry (wild type, WT), gD$^{d7\text{-}32}$ and gD$^{Mut\ (D215G/R222N/F223I)}$ at an multiplicity of infection (MOI) of 1, respectively. At 24 hpi, samples were collected for IFA and TEM analyses (Extended Data Fig. 10a). There was no difference between WT and gD$^{d7\text{-}32}$ (Extended Data Fig. 10b,c), thus excluding the requirement of HVEM and 3-O-sulfated heparan sulfate. The transsynaptic transmission deficit was observed only with gD$^{Mut\ (D215G/R222N/F223I)}$ (Extended Data Fig. 10b,c). This indicates that functional interaction between gD and nectin-1, rather than HVEM or 3-O-sulfated heparan sulfate, is essential for H129 transneuronal spread. Additionally, the TEM images showed that a WT virion was partially engulfed by the postsynaptic membrane (Fig. 6e). In contrast, gD$^{Mut\ (D215G/R222N/F223I)}$ virions remained near the synaptic cleft and could not enter the postsynaptic compartment (Fig. 6e–g). TMEFF1 was recently identified as a specific HSV restriction factor, whose interaction with nectin-1 could prevent gD from binding nectin-1 to suppress HSV-1 entry[41,42] and H129 transsynaptic spread. We knocked down TMEFF1 in postsynaptic neurons using rAAV2/9 vectors (Extended Data Fig. 10d–f), and found that it did not affect presynaptic viral production, but significantly enhanced the efficiency of H129 entry into the TMEFF1-knocked down postsynaptic neurons (Extended Data Fig. 10g–i). This result demonstrates that TMEFF1 restricts transsynaptic spread at the point of postsynaptic entry and strongly supports the conclusion that H129 uses a conserved, gD/nectin-1-dependent mechanism for transsynaptic invasion of downstream neurons.

After neurotransmission, endocytosis at the postsynaptic compartment is typically mediated by clathrin[43,44]. A clathrin-like structure was observed at the postsynaptic membrane engulfing a virion (Fig. 6e), indicating that H129 virions may also use clathrin-mediated endocytosis (CME) to enter postsynaptic neurons. Approximately 30% H129 particles colocalized with clathrin in the postsynaptic compartment (Fig. 6h–j). Moreover, TEM images showed that approximately 73% of viral particles in the postsynaptic compartment were enclosed within clathrin-coated vesicles (Fig. 6k,l).

To investigate the contribution of CME to the H129 entry of postsynaptic neurons, a selective inhibitor of CME, Pitstop2, was applied to neurons in the postsynaptic chamber[45] (Extended Data Fig. 10j). Pitstop2 significantly inhibited H129 transsynaptic transmission in a dose-dependent manner (Extended Data Fig. 10k,l). Virions being engulfed by the clathrin-coated postsynaptic membrane could be normally observed by TEM (Fig. 6m), but Pitstop2 treatment prevented virions from entering the postsynaptic neuron, leaving a greater number of virions in the perisynaptic cleft (Fig. 6n,o). These findings indicate that postsynaptic CME is essential for H129's transsynaptic entry into postsynaptic neurons.

To map the spatial organization of H129 transsynaptic transmission, we measured the distance from the H129 secretion site to the active zone, and from the postsynaptic CME site to the nearest PSD edge. These measurements were similar (230.3 ± 37.8 nm and 225.9 ± 30.7 nm, respectively), suggesting that H129 directly enters postsynaptic neurons (Fig. 6p). To account for variations in spine size, we calculate the CME positions relative to the PSD by normalizing the difference of the distances from each CME position to the nearest ($D1$) and farthest ($D2$) edges of the PSD along the plasma membrane ($D_N = 1 - \frac{|D1-D2|}{D1+D2}$; Fig. 6m), with 0 representing the PSD edge and 1.0 marking the point along the spine perimeter equidistant from both PSD edges[44]. These normalized data showed that H129 postsynaptic CME sites were concentrated near the PSD edge and were midway between the PSD edge and the farthest point along the perimeter, similar to the typical postsynaptic endocytic zone (Fig. 6q). These findings suggest that H129 postsynaptic entry through CME occurs at the peri-postsynaptic region relative to the presynaptic secretion position.

Fig. 6 | H129-gD and CME are necessary for H129 transsynaptically entering postsynaptic neurons at the peri-postsynaptic compartment. **a**–**c**, H129 colocalizes with PSD95 and nectin-1. **a**, Colocalization (white arrowheads) of VP26-mCherry, PSD95 and nectin-1 (magenta), with the dashed rectangle enlarged below. **b**, Normalized line profiles of intensity of VP26-mCherry, PSD95 and nectin-1. **c**, Percentage of VP26-mCherry^{+} with nectin-1^{+} and PSD95^{+} signals. **d**–**g**, gD/nectin-1 interaction and postsynaptic entry. **d**, Genomic diagram of H129 WT gD (gD^{WT}), gD$^{d7\text{-}32}$ and gD$^{Mut\ (D215G/R222N/F223I)}$. **e**,**f**, TEM images. H129 virion stopped at the perisynaptic cleft after infection with H129-VP26-mCherry (**e**, WT, red arrowheads, zoomed in on upright) and H129-VP26-mCherry-gD$^{Mut\ (D215G/R222N/F223I)}$ (**f**, gD$^{Mut\ (D215G/R222N/F223I)}$, white arrowhead). **g**, Percentage of H129 particles in different synaptic compartments in WT and gD$^{Mut\ (D215G/R222N/F223I)}$ groups. **h**–**l**, H129 postsynaptic entry and CME. **h**, Colocalization (white arrowheads, zoomed in on bottom) of VP26-mCherry, PSD95 and CHC1 (cyan). **i**, Normalized line profiles of intensity of VP26-mCherry, PSD95 and nectin-1. **j**, Percentage of VP26-mCherry^{+} with PSD95^{+} and CHC1^{+} signals. **k**, TEM images: H129 particles in the postsynaptic compartment (capsid, white arrowhead; virion in CCV, green arrowhead, zoomed in on upright). **l**, The percentage of capsid and virion in CCV in postsynaptic compartment. **m**–**q**, H129 postsynaptic endocytosis and Pitstop2 treatment. **m**, TEM images: H129 virion entering postsynaptic neuron with clathrin-coated pit (red arrowheads, zoomed in on downright). **n**, H129 virion is stopped at the perisynaptic cleft after Pitstop2 treatment (white arrowheads). **o**, Percentage of H129 particles in different synaptic compartments after Pitstop2 treatment. **p**, Measurement of the distance of the secretion site from the active zone and the distance of the endocytosis site from the PSD. **q**, Normalized tangential distributions of H129 CME ($D1$ and $D2$ in **m** are shown) were calculated as: $D_N = 1\frac{|D1-D2|}{D1+D2}$. Data are represented as mean ± s.e.m. CCV, clathrin-coated vesicle.

https://doi.org/10.1038/s41593-026-02254-8

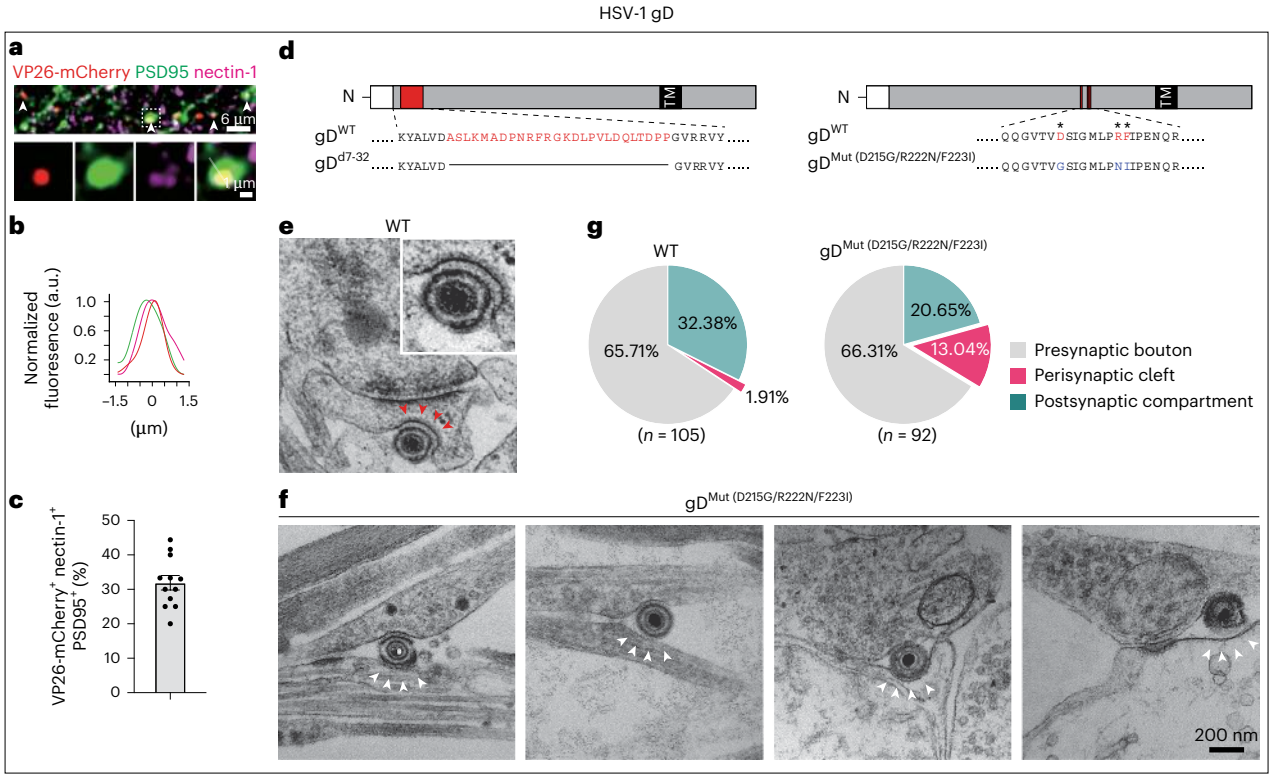

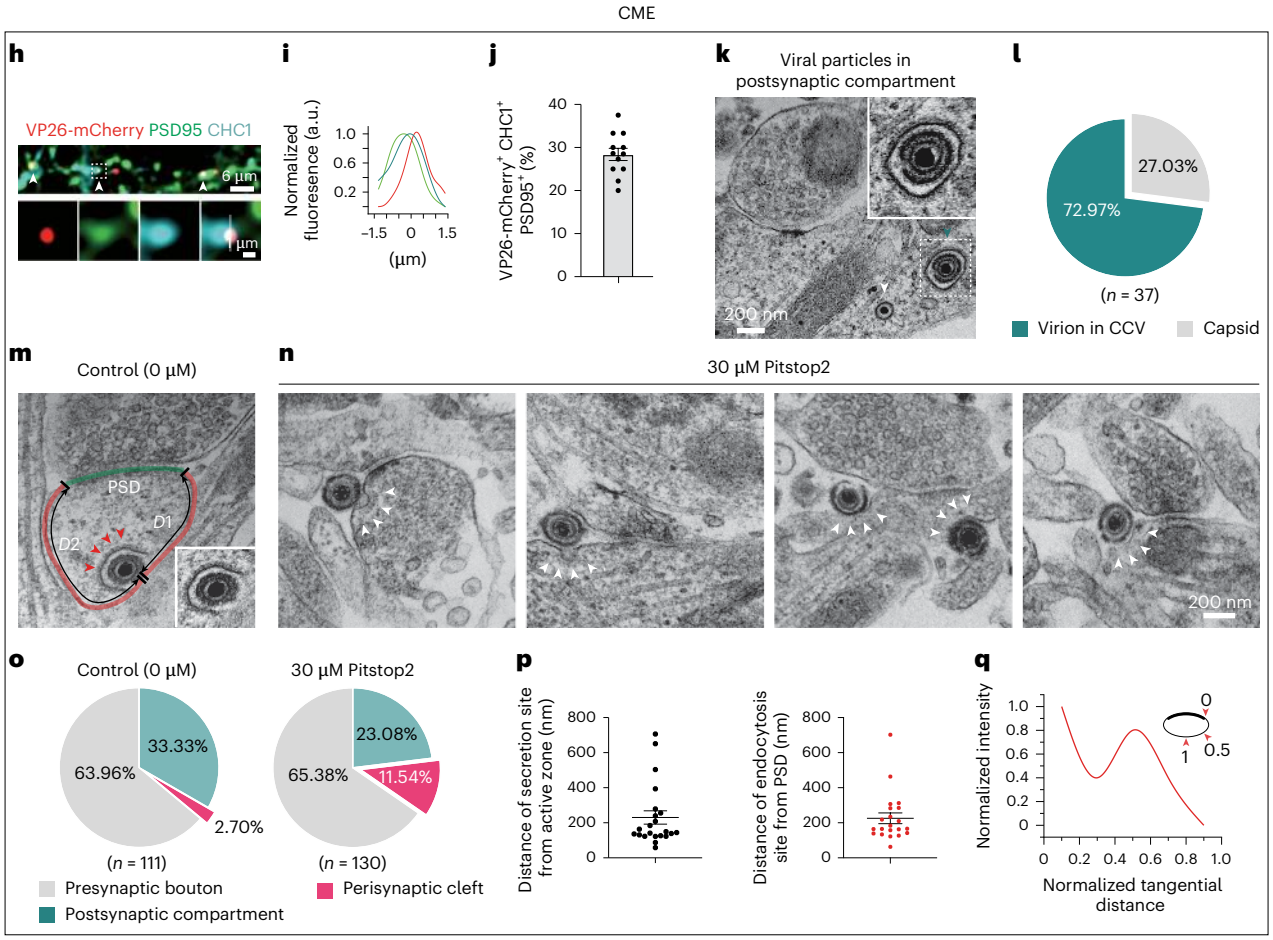

https://doi.org/10.1038/s41593-026-02254-8

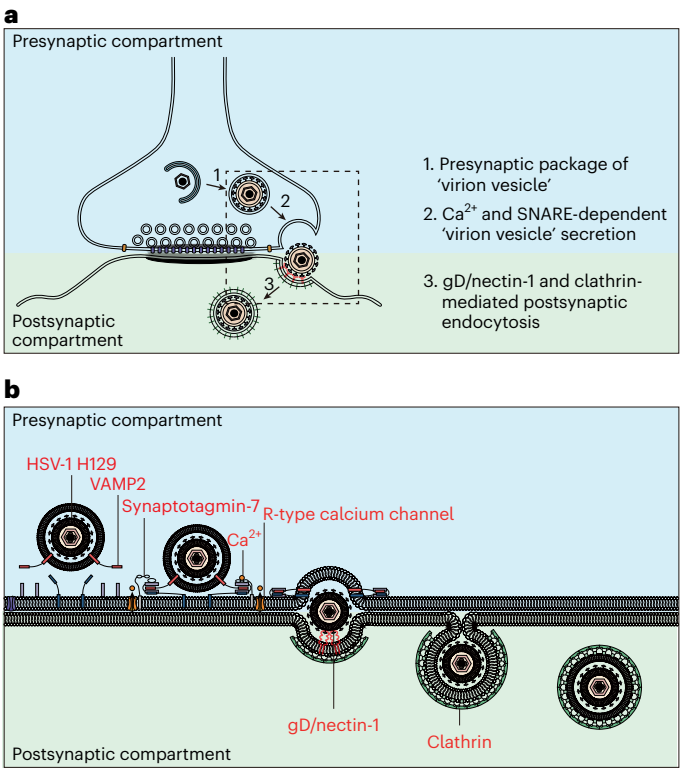

Fig. 7 | Working model of HSV-1 H129 transsynaptic transmission. a, Process of H129 transsynaptic transmission. (1) Packing H129 particle into 'virion vesicle' is required for exit from presynaptic bouton and further transsynaptically transmitting. (2) 'Virion vesicle' secretes from presynaptic bouton in a Ca^{2+} and SNARE-dependent manner, including voltage-gated Ca^{2+} channels, Syt7 and VAMP2. (3) H129 enters postsynaptic neurons through gD/nectin-1 and CME at perisynaptic compartment. **b**, The detailed molecular machinery of H129 transsynaptic transmission.

Discussion

We show that H129 transneuronal spread occurs by co-opting the molecular machinery of transsynaptic transmission—Ca^{2+}-dependent presynaptic secretion and clathrin-mediated postsynaptic endocytosis (Fig. 7). H129 capsids are packed into membrane-bound 'virion vesicles' in presynaptic boutons, primed for release, and secreted in an activity-dependent manner. Release requires Ca^{2+} influx through R-type channels and the SNARE machinery, including Syt7 and VAMP2, similar to DCV exocytosis. Once released, virions accumulate transiently in the perisynaptic cleft and are internalized rapidly by gD–nectin-1 interaction and CME.

Multiple observations support synapse-restricted transmission. First, H129 particles colocalize with synaptic markers (Fig. 1b–d), move across synapses (Fig. 1h–j) and detected by TEM in the perisynaptic cleft (average distance of presynaptic secretion site from active zone of 230.3 nm and average distance of postsynaptic endocytosis site from PSD of 225.9 nm; Figs. 1k, 3e and 6p). These results are consistent with our previous study showing that H129 particles tend to appear at axon terminals and varicosities[7]. Furthermore, the presynaptic secretion sites of H129 (230.3 nm) and DCVs (ranging 100–300 nm from the active zone) are spatially similar and predominantly surround the active zone[46].

Second, 'virion vesicle' assembly is essential for secretion. H129 particles colocalize and cotransport with the autophagy marker LC3b at the presynaptic boutons (Extended Data Fig. 4), and different states of autophagic engulfment of H129 capsids to form 'virion vesicles' are observed by TEM (Fig. 2c). Disrupting autophagic flux causes capsid accumulation, impairs vesicle formation in boutons and blocks transsynaptic spread (Fig. 2e–k). This supports that HSV-1 may complete its envelopment in varicosities and growth cones and then exit immediately there[10]. By packing capsids into 'virion vesicles', H129 gains similar features to the DCVs[47], which enables them to use their synaptic transmission machinery for secretion.

Third, their secretion dynamics further mirror neurotransmission[27,48], with rapid fusion followed by a slower and stable full secretion phase (Fig. 3e–h), and with strong dependence on neural activity and voltage-gated Ca^{2+} channels (Figs. 3i–n and 4d–r). Pharmacological blockage of R-type channels reduces postsynaptic infection and increases presynaptic 'virion vesicle' accumulation (Fig. 4n–r), in agreement with that R-type channels are activated by sustained activity and depolarization to elevate presynaptic residual calcium[49,50], which is also critical for DVCs' secretion. Consistent with this, loss or dysfunction of Syt7, which is a key Ca^{2+} sensor for both DCV release in neuroendocrine cells[51] and asynchronous release in hippocampal neurons[52], suppresses H129 spread and traps vesicles in boutons (Fig. 5b–f), and rescue requires intact Ca^{2+} binding, indicating that Syt7 functions as a Ca^{2+} sensor for H129 secretion. Additionally, pharmacological blockage and genetic knockdown of VAMP2 also suppress H129 secretion (Fig. 5g–p), implicating canonical SNARE-mediated fusion similar to vesicle release. It is in agreement with previous studies that VAMP2 cotransports with HSV-1 particles in the axon[15] and supports H129 secretion.

Meanwhile, H129 enters the postsynaptic endocytic zone immediately after presynaptic secretion through CME at the peri-PSD endocytic zone (Fig. 6). gD/nectin-1 interaction is essential for H129 to enter postsynaptic neurons transsynaptically, whereas HVEM and 3-O-sulfated heparan sulfate are not required. H129-VP26-mCherry-gD$^{Mut\ (D215G/R222N/F223I)}$ causes a remarkable impairment in transsynaptic spread and an accumulation of virions in the perisynaptic cleft (Extended Data Fig. 10a–c and Fig. 6d–g), and TMEFF1 knockdown in postsynaptic neurons increased transsynaptic infection (Extended Data Fig. 10d–i). Therefore, nectin-1 is necessary for HSV-1 entry into neurons during both primary infection and transsynaptic transmission. H129 enters the postsynaptic endocytic zone through a classic clathrin-dependent process like typical postsynaptic receptor endocytosis[43,44]. Virions are detected in clathrin-coated vesicles and colocalize with clathrin heavy chain, and Pitstop2 suppresses transsynaptic infection while increasing cleft-resident virions (Fig. 6h–o). Overall, our results, together with previous findings, support that gD/nectin-1 and CME are necessary molecular components for H129 postsynaptic entry and transsynaptic transmission.

Together, these results establish that H129 hijacks synaptic secretion and endocytosis to move across synaptically connected neurons. This synapse-specific mechanism clarifies the direction specificity of H129-derived anterograde tracers to map circuits and suggests strategies to tune tracer performance by selectively modulating transsynaptic transmission without altering local replication. More notably, insights into these mechanisms deepen our understanding of HSV-1 spread within the CNS, which causes life-threatening herpetic encephalitis, recurrent herpes and the potential transsynaptic pathological cascade to increase risk factor of AD[1,3], and may also shed light on interventions that disrupt pathological propagation while preserving synaptic function.

Online content

Any methods, additional references, Nature Portfolio reporting summaries, source data, extended data, supplementary information, acknowledgements, peer review information; details of author contributions and competing interests; and statements of data and code availability are available at https://doi.org/10.1038/s41593-026-02254-8.

References

1. Marcocci, M. E. et al. Herpes simplex virus-1 in the brain: the dark side of a sneaky infection. *Trends Microbiol.* **28**, 808–820 (2020).
2. Griffin, D. E. Viral encephalomyelitis. *PLoS Pathog.* **7**, e1002004 (2011).

3. Ball, M. J., Lukiw, W. J., Kammerman, E. M. & Hill, J. M. Intracerebral propagation of Alzheimer's disease: strengthening evidence of a herpes simplex virus etiology. *Alzheimers Dement.* **9**, 169–175 (2013).
4. Ugolini, G., Kuypers, H. G. & Strick, P. L. Transneuronal transfer of herpes virus from peripheral nerves to cortex and brainstem. *Science* **243**, 89–91 (1989).
5. Pegg, C. E. et al. Herpesviruses assimilate kinesin to produce motorized viral particles. *Nature* **599**, 662–666 (2021).
6. DuRaine, G., Wisner, T. W., Howard, P. & Johnson, D. C. Kinesin-1 proteins KIF5A, -5B, and -5C promote anterograde transport of herpes simplex virus enveloped virions in axons. *J. Virol.* **92**, e01269-18 (2018).
7. Dong, X. et al. Anterograde viral tracer herpes simplex virus 1 strain H129 transports primarily as capsids in cortical neuron axons. *J. Virol.* **94**, e01957-19 (2020).
8. Wong, M. Y. et al. Neuropeptide delivery to synapses by long-range vesicle circulation and sporadic capture. *Cell* **148**, 1029–1038 (2012).
9. Taylor, M. P. & Enquist, L. W. Axonal spread of neuroinvasive viral infections. *Trends Microbiol.* **23**, 283–288 (2015).
10. Saksena, M. M. et al. Herpes simplex virus type 1 accumulation, envelopment, and exit in growth cones and varicosities in mid-distal regions of axons. *J. Virol.* **80**, 3592–3606 (2006).
11. Danastas, K. et al. Herpes simplex virus-1 utilizes the host actin cytoskeleton for its release from axonal growth cones. *PLoS Pathog.* **18**, e1010264 (2022).
12. Ambrosini, A. E. et al. Alpha herpesvirus exocytosis from neuron cell bodies uses constitutive secretory mechanisms, and egress and spread from axons is independent of neuronal firing activity. *PLoS Pathog.* **20**, e1012139 (2024).
13. Li, E. et al. Anterograde transneuronal tracing and genetic control with engineered yellow fever vaccine YFV-17D. *Nat. Methods* **18**, 1542–1551 (2021).
14. Piacentini, R. et al. HSV-1 promotes Ca^{2+}-mediated APP phosphorylation and Aβ accumulation in rat cortical neurons. *Neurobiol. Aging* **32**, 2323 (2011).
15. Antinone, S. E., Zaichick, S. V. & Smith, G. A. Resolving the assembly state of herpes simplex virus during axon transport by live-cell imaging. *J. Virol.* **84**, 13019–13030 (2010).
16. Dix, R. D., McKendall, R. R. & Baringer, J. R. Comparative neurovirulence of herpes simplex virus type 1 strains after peripheral or intracerebral inoculation of BALB/c mice. *Infect. Immun.* **40**, 103–112 (1983).
17. Zeng, W. B. et al. Anterograde monosynaptic transneuronal tracers derived from herpes simplex virus 1 strain H129. *Mol Neurodegener.* **12**, 38 (2017).
18. Zemanick, M. C., Strick, P. L. & Dix, R. D. Direction of transneuronal transport of herpes simplex virus 1 in the primate motor system is strain-dependent. *Proc. Natl Acad. Sci. USA* **88**, 8048–8051 (1991).
19. Lo, L. & Anderson, D. J. A Cre-dependent, anterograde transsynaptic viral tracer for mapping output pathways of genetically marked neurons. *Neuron* **72**, 938–950 (2011).
20. Yang, H. et al. A novel H129-based anterograde monosynaptic tracer exhibits features of strong labeling intensity, high tracing efficiency, and reduced retrograde labeling. *Mol Neurodegener.* **17**, 6 (2022).
21. Chen, T. et al. The role of autophagy in viral infections. *J. Biomed. Sci.* **30**, 5 (2023).
22. Cocchi, F. et al. The soluble ectodomain of herpes simplex virus gD contains a membrane-proximal pro-fusion domain and suffices to mediate virus entry. *Proc. Natl Acad. Sci. USA* **101**, 7445–7450 (2004).
23. Paroutis, P., Touret, N. & Grinstein, S. The pH of the secretory pathway: measurement, determinants, and regulation. *Physiology* **19**, 207–215 (2004).
24. Miesenbock, G., De Angelis, D. A. & Rothman, J. E. Visualizing secretion and synaptic transmission with pH-sensitive green fluorescent proteins. *Nature* **394**, 192–195 (1998).
25. Liu, Y. T. et al. Biphasic exocytosis of herpesvirus from hippocampal neurons and mechanistic implication to membrane fusion. *Cell Discov.* **6**, 2 (2020).
26. Avinoam, O., Schorb, M., Beese, C. J., Briggs, J. A. & Kaksonen, M. ENDOCYTOSIS. Endocytic sites mature by continuous bending and remodeling of the clathrin coat. *Science* **348**, 1369–1372 (2015).
27. Brunger, A. T., Choi, U. B., Lai, Y., Leitz, J. & Zhou, Q. Molecular mechanisms of fast neurotransmitter release. *Annu. Rev. Biophys.* **47**, 469–497 (2018).
28. Granstedt, A. E., Bosse, J. B., Thiberge, S. Y. & Enquist, L. W. In vivo imaging of αherpesvirus infection reveals synchronized activity dependent on axonal sorting of viral proteins. *Proc. Natl Acad. Sci. USA* **110**, E3516–E3525 (2013).
29. De Luca, A. et al. Effects of omega-conotoxin GVIA on autonomic neuroeffector transmission in various tissues. *Br. J. Pharmacol.* **101**, 437–447 (1990).
30. Mintz, I. M. et al. P-type calcium channels blocked by the spider toxin omega-Aga-IVA. *Nature* **355**, 827–829 (1992).
31. Newcomb, R. et al. Selective peptide antagonist of the class E calcium channel from the venom of the tarantula Hysterocrates gigas. *Biochemistry* **37**, 15353–15362 (1998).
32. Dreyfus, F. M. et al. Selective T-type calcium channel block in thalamic neurons reveals channel redundancy and physiological impact of I(T)window. *J. Neurosci.* **30**, 99–109 (2010).
33. Hof, R. P., Salzmann, R. & Siegl, H. Selective effects of PN 200-110 (isradipine) on the peripheral circulation and the heart. *Am. J. Cardiol.* **59**, 30B–36B (1987).
34. Sakaba, T., Stein, A., Jahn, R. & Neher, E. Distinct kinetic changes in neurotransmitter release after SNARE protein cleavage. *Science* **309**, 491–494 (2005).
35. Schiavo, G. et al. Tetanus and botulinum-B neurotoxins block neurotransmitter release by proteolytic cleavage of synaptobrevin. *Nature* **359**, 832–835 (1992).
36. Campadelli-Fiume, G., Cocchi, F., Menotti, L. & Lopez, M. The novel receptors that mediate the entry of herpes simplex viruses and animal αherpesviruses into cells. *Rev. Med. Virol.* **10**, 305–319 (2000).
37. Mizoguchi, A. et al. Nectin: an adhesion molecule involved in formation of synapses. *J. Cell Biol.* **156**, 555–565 (2002).
38. Generous, A. R. et al. Trans-endocytosis elicited by nectins transfers cytoplasmic cargo, including infectious material, between cells. *J. Cell Sci.* **132**, jcs235507 (2019).
39. Yoon, M., Zago, A., Shukla, D. & Spear, P. G. Mutations in the N termini of herpes simplex virus type 1 and 2 gDs alter functional interactions with the entry/fusion receptors HVEM, nectin-2, and 3-O-sulfated heparan sulfate but not with nectin-1. *J. Virol.* **77**, 9221–9231 (2003).
40. Manoj, S., Jogger, C. R., Myscofski, D., Yoon, M. & Spear, P. G. Mutations in herpes simplex virus glycoprotein D that prevent cell entry via nectins and alter cell tropism. *Proc. Natl Acad. Sci. USA* **101**, 12414–12421 (2004).
41. Chan, Y. H. et al. Human TMEFF1 is a restriction factor for herpes simplex virus in the brain. *Nature* **632**, 390–400 (2024).
42. Dai, Y. et al. TMEFF1 is a neuron-specific restriction factor for herpes simplex virus. *Nature* **632**, 383–389 (2024).
43. Lu, J. et al. Postsynaptic positioning of endocytic zones and AMPA receptor cycling by physical coupling of dynamin-3 to Homer. *Neuron* **55**, 874–889 (2007).
44. Racz, B., Blanpied, T. A., Ehlers, M. D. & Weinberg, R. J. Lateral organization of endocytic machinery in dendritic spines. *Nat. Neurosci.* **7**, 917–918 (2004).

45. Von Kleist, L. et al. Role of the clathrin terminal domain in regulating coated pit dynamics revealed by small molecule inhibition. *Cell* **146**, 471–484 (2011).
46. Mansvelder, H. D. & Kits, K. S. Calcium channels and the release of large dense core vesicles from neuroendocrine cells: spatial organization and functional coupling. *Prog. Neurobiol.* **62**, 427–441 (2000).
47. Van Westen, R., Poppinga, J., Diez Arazola, R., Toonen, R. F. & Verhage, M. Neuromodulator release in neurons requires two functionally redundant calcium sensors. *Proc. Natl Acad. Sci. USA* **118**, e2012137118 (2021).
48. Sudhof, T. C. The synaptic vesicle cycle. *Annu. Rev. Neurosci.* **27**, 509–547 (2004).
49. Li, L., Bischofberger, J. & Jonas, P. Differential gating and recruitment of P/Q-, N-, and R-type Ca^{2+} channels in hippocampal mossy fiber boutons. *J. Neurosci.* **27**, 13420–13429 (2007).
50. Dietrich, D. et al. Functional specialization of presynaptic Cav2.3 Ca^{2+} channels. *Neuron* **39**, 483–496 (2003).
51. Schonn, J. S., Maximov, A., Lao, Y., Sudhof, T. C. & Sorensen, J. B. Synaptotagmin-1 and -7 are functionally overlapping Ca^{2+} sensors for exocytosis in adrenal chromaffin cells. *Proc. Natl Acad. Sci. USA* **105**, 3998–4003 (2008).
52. Bacaj, T. et al. Synaptotagmin-1 and synaptotagmin-7 trigger synchronous and asynchronous phases of neurotransmitter release. *Neuron* **80**, 947–959 (2013).

[1]State Key Laboratory of Virology and Biosafety, CAS Center for Excellence in Brain Science and Intelligence Technology, Wuhan Institute of Virology, Chinese Academy of Sciences, Wuhan, China. [2]University of Chinese Academy of Sciences, Beijing, China. [3]State Key Laboratory of Magnetic Resonance Spectroscopy and Imaging, National Center for Magnetic Resonance in Wuhan, Innovation Academy for Precision Measurement Science and Technology, Chinese Academy of Sciences, Wuhan, China. [4]Center for Neural Circuit Mapping, Department of Physiology and Biophysics, School of Medicine, University of California, Irvine, Irvine, CA, USA. [5]Guangdong Provincial Key Laboratory of Infection Immunity and Inflammation, Department of Pathogen Biology, Shenzhen University Medical School, Shenzhen, China. [6]Research Center of Biomedical Engineering, School of Life Health Information Science and Engineering, University of Posts and Telecommunications, Chongqing, China. [7]Department of Neurobiology, School of Basic Medicine, Tongji Medical College, Huazhong University of Science and Technology, Wuhan, China. ✉e-mail: xiongfeng@apm.ac.cn; xinzhou@wipm.ac.cn; zengwb@wh.iov.cn; xingliu1@szu.edu.cn; zhaocongjian@cqupt.edu.cn; yhan@hust.edu.cn; luomh@wh.iov.cn

Methods

All experimental procedures were approved by the Institutional Review Board and Institutional Animal Welfare Committee of Wuhan Institute of Virology, Chinese Academy of Sciences (WIVA10202001). All experiments with viruses were approved by the Institutional Biosafety Committee and performed in Biosafety Level 2 laboratory following the institutionally approved standard operating procedures and biosafety guidelines.

Cells

Vero-E6 and Vero-gD cells were used for virus propagation of H129 recombinants applied in this study. Vero-E6 cells (ATCC-CRL 1586, purchased from ATCC) were maintained in our laboratory. Vero-gD cell line, stably expressing WT H129 glycoprotein D (gD^{WT}), was generated by lentivirus-gD^{WT} transduction[53]. Briefly, gD^{WT} coding gene was inserted into the lentivirus vector to generate the pCDH-gD^{WT}-puro expression vector. The rAAV2/9 and lentivirus were packaged in HEK293T (ATCC-CRL 11268, kept in our lab) as described previously, and then used to transduce Vero-E6 cells and neurons[54,55]. The transduced cells were selected with 4 μg ml^{-1} puromycin for 14 days, and then maintained under the selection pressure of 2 μg ml^{-1} puromycin. All these cells were cultured with DMEM containing 10% FBS and 1% penicillin–streptomycin in the incubator with 5% CO_2 at 37 °C.

Microfluidic chamber fabrication

The microfluidic plates were fabricated following the protocol as previously described[56,57], and the parameters of the microgrooves mask and chamber mask were designed accordingly[17]. Then the masks were produced by Microclear Electronics Technology. Photoresist SU-8 GM1050, GM1075 (Gersteltec Sarl) and propylene glycol methyl ether acetate (Sigma) were used to fabricate the plate of the microfluidic chamber. The microgrooves of the plate are 700 μm in length, 10 μm in width and 3 μm in depth. Finally, polydimethylsiloxane (Sylgard 184, Dow Corning) was used to produce the microfluidic chamber.

Primary mouse cortical neurons isolation and culture in the microfluidic chamber

Primary mouse cortical neurons were prepared from embryonic day 16.5 (E16.5) C57BL/6 mouse embryos according to the protocol as described previously[7,17]. Dissected cortical tissues were digested with 0.125% trypsin and 0.01% DNase I in HBSS containing 1 mM HEPES, 10 mM sodium pyruvate, 3% D-(+)-glucose and 1% penicillin–streptomycin at 37 °C for 15 min. Cell pellets were washed with neurobasal medium supplemented with 2% B27 supplement and GlutaMAX, dissociated by passing through plastic pipette tips. Then, cortical neurons were plated in ploy-D-lysine (0.1 mg ml^{-1}) coated dish with the microfluidic chamber at a density of 1×10^6 neurons per side. The medium was changed every day during the culture process.

Construction of recombinant tool viruses

All the recombinant viruses used in this study were derived from the previously established H129-VP26-mCherry, in which the small capsid protein VP26 is fused with mCherry[7]. Using bacterial artificial chromosome and homologous recombination techniques[58], a CMV-promoter (pCMV) controlled expression cassette for synaptophysin-BFP was inserted into the H129-VP26-mCherry genome at the specified position, creating H129-VP26-mCherry-syBFP. Following the same approach, P2A-eGFP-LC3b was added after BFP based on H129-VP26-mCherry-syBFP, resulting in H129-VP26-mCherry-syBFP-P2A-eGFP-LC3b. Superecliptic pHluorin was fused to the N terminus of the H129-VP26-mCherry glycoprotein D, generating H129-VP26-mCherry-pHluorin-gD. The coding sequence for amino acids 7-32 of gD was replaced with null homologous arms to generate H129-VP26-mCherry-$gD^{d7\text{-}32}$. Subsequently, the amino acid sequence 215-223 of gD was replaced with a mutant sequence to produce H129-VP26-mCherry-$gD^{Mut\ (D215G/R222N/F223I)}$. Based on H129-VP26-mCherry-syBFP, syBFP was replaced with syGCaMP3.5 to create H129-VP26-mCherry-syGCaMP3.5. Similarly, the U6-promoter (pU6) controlled shRNA expression cassette was inserted into the H129-VP26-mCherry genome at the indicated position to generate H129-VP26-mCherry-sh (knockdown vector). The following shRNA sequences were used: scramble, 5′-CCTAAGGTTAAGTCGCCCTCG-3′[59]; Syt1, 5′-GAGCAAATCCAGAAAGTG CAA-3′[60]; Syt7, 5′-GATCT ACCTGTCCTGGAAGAG-3′[52]; VAMP2, 5′-GGACCAGAAGTTGT CGGAGCT-3′[61]; TMEFF1, 5′-GCTCACCCATGTTCTTATCGC-3′[62]. Additionally, EF1a-promoter (pEF1a) controlled $Syt7^{WT}$ (NM_021659) and $Syt7^{C2A*B*}$ (ref. 52) were inserted downstream of the shRNA at the indicated position to create H129-VP26-mCherry-shR (knockdown-rescue vector), respectively. All these recombinant viral genome modifications were performed in *Escherichia coli* strains DY380 or SW102 using homologous recombination and validated by PCR and sequencing. H129-VP26-mCherry-syBFP, H129-VP26-mCherry-syBFP-P2A-eGFP-LC3b, H129-VP26-mCherry-pHluorin-gD, H129-VP26-mCherry-syGCaMP3.5, H129-VP26-mCherry-sh and H129-VP26-mCherry-shR were reconstituted and propagated in Vero-E6 cells, while H129-VP26-mCherry-$gD^{d7\text{-}32}$ and H129-VP26-mCherry-$gD^{Mut\ (D215G/R222N/F223I)}$ were reconstituted and propagated in cell line Vero-gD, which expresses the gD^{wt}.

Preparation of cell-free virus stock

Vero-E6 and Vero-gD were infected with the recombinant viruses at an MOI of 0.1 in T175 flasks, respectively. The culture media were collected when 100% cells displayed severe cytopathic effects at 48 hpi. By centrifuging for 10 min at 380*g* and 4 °C to remove cell debris, the supernatant was collected and subjected to ultracentrifugation (Beckman rotor SW32; 107,000*g*, 2.5 h, 4 °C). Pellets were resuspended in DMEM, aliquoted 5–10 μl per vial, and stored at −80 °C. Titers of cell-free virus stocks were determined by plaque-forming assay after thaw. The titers of these recombinant viruses range from 2×10^9 to 5×10^9 PFU ml^{-1}, which are similar to those of the WT H129.

IFA

Neurons cultured in microfluidic chamber were washed with sterile PBS and then fixed with 4% paraformaldehyde at room temperature for 15 min. After washing, samples were blocked with 0.4% Triton X-100, 1% BSA and 4% goat serum in PBS for 60 min. Primary antibodies specific for synaptobrevin-2 (VAMP2, 1:1,000, IgG1; 104211, Synaptic System), STX-1 (1:500, IgG1; 110011, Synaptic System), PSD95 (1:500, IgG2a; 75-028, NeuroMab), synaptotagmins-1 (1:200, IgG2a; 105011, Synaptic System), synaptotagmins-7 (1:500, rabbit polyclonal; 105173, Synaptic System), LC3b (1:500, rabbit polyclonal; 4108, Cell Signaling Technology), nectin-1 (1:500, rabbit polyclonal; ab229464, Abcam), TMEFF1 (1:100, IgG2b; sc-393457, Santa Cruz Biotechnology) and CHC1 (1:500, rabbit polyclonal; ab21679, Abcam) were incubated overnight at 4 °C. After washing, secondary antibodies were incubated at room temperature for 60 min. Finally, after 10 min of DAPI staining (1:1,000), the samples were cover-slipped with mounting media.

Live imaging

Live imaging was performed during 16–24 hpi with a Leica ×60/1.40 oil objective on the spinning-disk confocal microscope (Andor Dragonfly 202, Oxford Instruments) at 37 °C with 5% CO_2 in an enclosed culture chamber. The acquisition frequency of H129-VP26-mCherry-syBFP traffic across synapse, H129-VP26-mCherry-syBFP-P2A-eGFP-LC3b cotransportation and H129-VP26-mCherry-pHluorin-gD presynaptic secretion were 0.5 Hz; H129-VP26-mCherry-syGCaMP3.5 presynaptic calcium transient was 5 Hz. All images were corrected by ImageJ (v2.9.0) plugins of 'Bleach Correction' and 'StackReg'. Fluorescence intensity (F) at the time point (t) was normalized by the intensity at $t = 0$ and shown as $dF/F_0 = (F(t) - F_0)/F_0$.

TEM

Neurons cultured in microfluidic chamber on a 35-mm confocal dish were washed with sterile 1× PBS and then fixed with 2.5% glutaraldehyde in situ at room temperature for 45 min. After washing with PBS, the samples were postfixed with 1% osmium tetroxide for 15 min and dehydrated with ethanol of ascending purity (30%, 50%, 70%, 80%, 85%, 90%, 95% and 100%) for 5 min at each concentration. Then, the resin was added for primary penetration at 37 °C for 4–6 h. Finally, fresh resin was replaced, and the sample was embedded at 60 °C for 48 h; the glass bottom was then broken using liquid nitrogen for ultrathin sectioning. Next, ultrathin sections (80 nm) were sequentially stained with 3.5% aqueous uranyl acetate and 0.2% lead citrate. Images were acquired on FEI Tecnai G^2 20 TWIN transmission electron microscope (Hillsboro).

Whole-cell patch clamp recording

The electrophysiological properties of the AP fired pattern and the membrane potential of cultured neurons in a microfluidic chamber were recorded by whole-cell patch clamp with Multiclamp 700B amplifiers and pCLAMP (v10.3). The internal solution in recording electrodes contains 140 mM potassium gluconate, 10 mM HEPES, 0.2 mM EGTA, 2 mM NaCl, 2 mM MgATP and 0.3 mM Na_2GTP. The external recording solution contains 145 mM NaCl, 4 mM KCl, 10 mM HEPES, 10 mM glucose, 2 mM $CaCl_2$ and 1 mM $MgCl_2$. Resting membrane potential was measured immediately after establishing the whole-cell configuration. APs were obtained by injecting 500 ms current steps that ranged from −80 pA to 300 pA, with a step size of 20 pA.

Statistics and reproducibility

For colocalization analysis, all IFA data were collected from at least four independent experiments using four different batches of primary neurons cultured in microfluidic chambers. Each independent experiment was performed in technical triplicate using the same batch of cultured neurons, and at least three fields of view per technical replicate were analyzed. For the TEM analysis (including pie charts and bar graphs), results were pooled from three independent experiments using three separate batches of cultured neurons. Each biological replicate included three technical repeats, and at least two sample positions near the postsynaptic microgrooves were processed for in situ slicing in each technical repeat. From each position, a minimum of three ultrathin sections were prepared, and dozens of fields of view per slice were imaged and analyzed. The results were presented as mean ± s.e.m. Student's *t* test, one-way analysis of variance (Tukey test) and Mann–Whitney *U* test were used to analyze the statistical significance among data groups. All statistical analyses were performed using GraphPad Prism (v9.4.1). The distributions of pore membrane angle and depth of the secretion cavity were analyzed by Origin Pro 2019b (v9.6.5). The detailed statistical reports for each figure are provided in the source data file, organized by figure and extended figure data. No statistical methods were used to predetermine sample sizes; sample sizes were chosen based on previous similar studies[7,17,20]. Data distribution was assumed to be normal, but this was not formally tested, and individual data points are shown where applicable. Data collection was randomized. Data collection and analysis were not performed blindly to the conditions of the experiments. No data points have been excluded from the analyses.

Reporting summary

Further information on research design is available in the Nature Portfolio Reporting Summary linked to this article.

Data availability

Data underlying Figs. 1–6 and Extended Data Figs. 1–10 are provided with the paper. Source data are provided with this paper.

Code availability

No custom software codes were used in the data analysis for this paper.

References

53. Ligas, M. W. & Johnson, D. C. A herpes simplex virus mutant in which glycoprotein D sequences are replaced by β-galactosidase sequences binds to but is unable to penetrate into cells. *J. Virol.* **62**, 1486–1494 (1988).
54. Xiong, F. et al. An HSV-1-H129 amplicon tracer system for rapid and efficient monosynaptic anterograde neural circuit tracing. *Nat. Commun.* **13**, 7645 (2022).
55. Wang, X. Z. et al. Human cytomegalovirus pUL97 upregulates SOCS3 expression via transcription factor RFX7 in neural progenitor cells. *PLoS Pathog.* **19**, e1011166 (2023).
56. Park, J. W., Vahidi, B., Taylor, A. M., Rhee, S. W. & Jeon, N. L. Microfluidic culture platform for neuroscience research. *Nat. Protoc.* **1**, 2128–2136 (2006).
57. Harris, J. et al. Fabrication of a microfluidic device for the compartmentalization of neuron soma and axons. *J. Vis. Exp.* **7**, 261 (2007).
58. Sharan, S. K., Thomason, L. C., Kuznetsov, S. G. & Court, D. L. Recombineering: a homologous recombination-based method of genetic engineering. *Nat. Protoc.* **4**, 206–223 (2009).
59. Sarbassov, D. D., Guertin, D. A., Ali, S. M. & Sabatini, D. M. Phosphorylation and regulation of Akt/PKB by the rictor-mTOR complex. *Science* **307**, 1098–1101 (2005).
60. Xu, W. et al. Distinct neuronal coding schemes in memory revealed by selective erasure of fast synchronous synaptic transmission. *Neuron* **73**, 990–1001 (2012).
61. Fan, H. P., Fan, F. J., Bao, L. & Pei, G. SNAP-25/syntaxin 1A complex functionally modulates neurotransmitter γ-aminobutyric acid reuptake. *J. Biol. Chem.* **281**, 28174–28184 (2006).
62. Nie, X. et al. Overexpression of TMEFF1 in endometrial carcinoma and the mechanism underlying its promotion of malignant behavior in cancer cells. *J. Cancer* **12**, 5772–5788 (2021).

Acknowledgements

The authors appreciate the Center for Experimental Animal, the Center for Instrumental Analysis and Metrology, and the Institutional Center for Shared Technologies and Facilities of the Wuhan Institute of Virology, Chinese Academy of Sciences, for their support with animal experiments and imaging. This work was supported by National Key R&D Program (2023YFC2306600 to M.-H.L. and W.-B.Z. and 2024YFA1803200 to Y.H.), National Natural Science Foundation of China (82430070 to M.-H.L., 32371148 to W.-B.Z., 32300147 to F.X., 32271082 to Y.H. and 82441015 to X.Z.), XD Project (XDB1610000 to M.-H.L.), Key R&D Program of Wuhan Municipality (2025020602030101 to M.-H.L.), Hubei Provincial Natural Science Foundation (2022CFA067 to Y.H.), Major Scientific Research Facility Project of Jiangsu Province (BM2022010 to Y.H.) and Interdisciplinary Research Program of HUST (2024JCYJ007 to Y.H.).

Author contributions

H.-B.Q., T.C.H., X.L., C.-J.Z., Y.H. and M.-H.L. wrote the paper with contributions of data from all co-authors. H.-B.Q. performed the experiments, obtained the images, analyzed the data and prepared the figures. Y.W. helped with the package and production of rAAV2/9. Y.-P.Z., T.-X.J., A.-N.D., D.G., J.-Y.S., X.-Z.J., Z.-Y.X. and Z.-Y.L. helped with the experiments. M.-H.L., Y.H., C.-J.Z., X.L., W.-B.Z., X.Z. and F.X. supervised the project. All authors read and approved the final paper.

Competing interests

All authors declare no competing interests.

Additional information

Extended data is available for this paper at https://doi.org/10.1038/s41593-026-02254-8.

Supplementary information The online version contains supplementary material available at https://doi.org/10.1038/s41593-026-02254-8.

Correspondence and requests for materials should be addressed to Feng Xiong, Xin Zhou, Wen-Bo Zeng, Xing Liu, Cong-Jian Zhao, Yunyun Han or Min-Hua Luo.

Peer review information *Nature Neuroscience* thanks Søren Paludan and the other, anonymous, reviewer(s) for their contribution to the peer review of this work.

https://doi.org/10.1038/s41593-026-02254-8

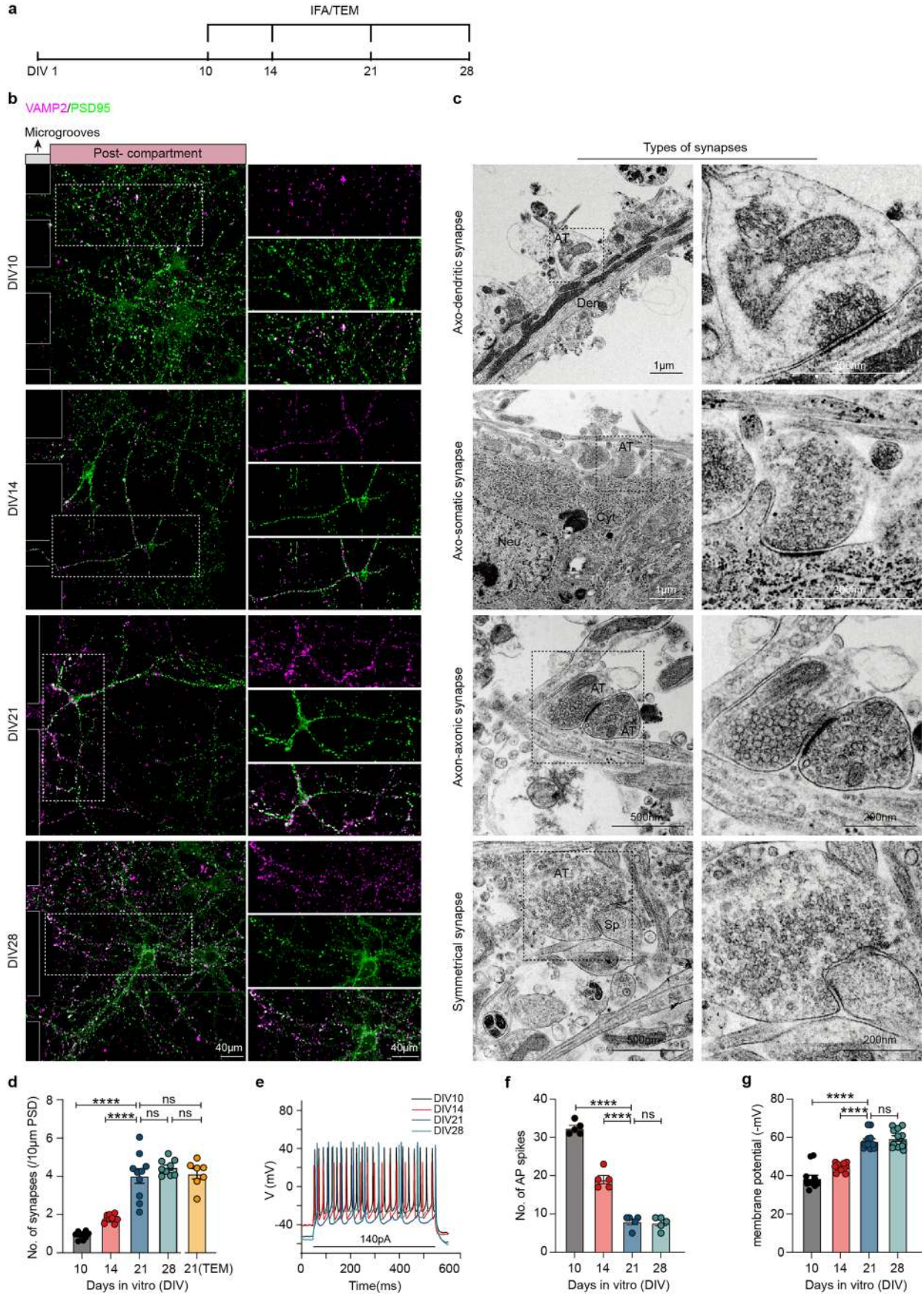

Extended Data Fig. 1 | See next page for caption.

https://doi.org/10.1038/s41593-026-02254-8

Extended Data Fig. 1 | Neurons cultured in a microfluidic chamber stabilize by DIV21 exhibiting consistent synapse density and response. a, Timeline depicting the experiment flow. **b**–**d**, Synapse density of neurons cultured in the microfluidic chamber. **b**, Confocal images show VAMP2 (magenta) and PSD95 (green) colocalizing at different times. Solid line marks microgroove borders; dashed rectangle (right panel) shows VP26-mCherry signal only. **c**, TEM images of different synapse types of DIV21 cultured neurons. The asymmetrical synapses, including axo-dendritic (first panel), axo-somatic (the second panel) and axo-axonic synapse (the third panel), and the symmetrical synapse (fourth panel) are shown. **d**, Quantification of synapse density. Synapse density was quantified based on IFA and TEM data shown in **b** and **c**, shown as the first four columns and the last column correspondingly. Data were analyzed by one-way ANOVA, Tukey test. **e**–**g**, Action potential firing pattern and membrane potential. **e**, Traces show the AP firing pattern as a response to step current injections (140pA, 500 ms) during the indicated culture times. Quantification of fire rate (**f**) and membrane potential (**g**). Data were analyzed by one-way ANOVA, Tukey test. Data are represented as mean ± s.e.m. ns: no significant and ****$p < 0.0001$. AT, axon terminal; Den, Dendrite; Cyt, cytoplasm; Neu, nucleus; Sp, dendritic spine.

https://doi.org/10.1038/s41593-026-02254-8

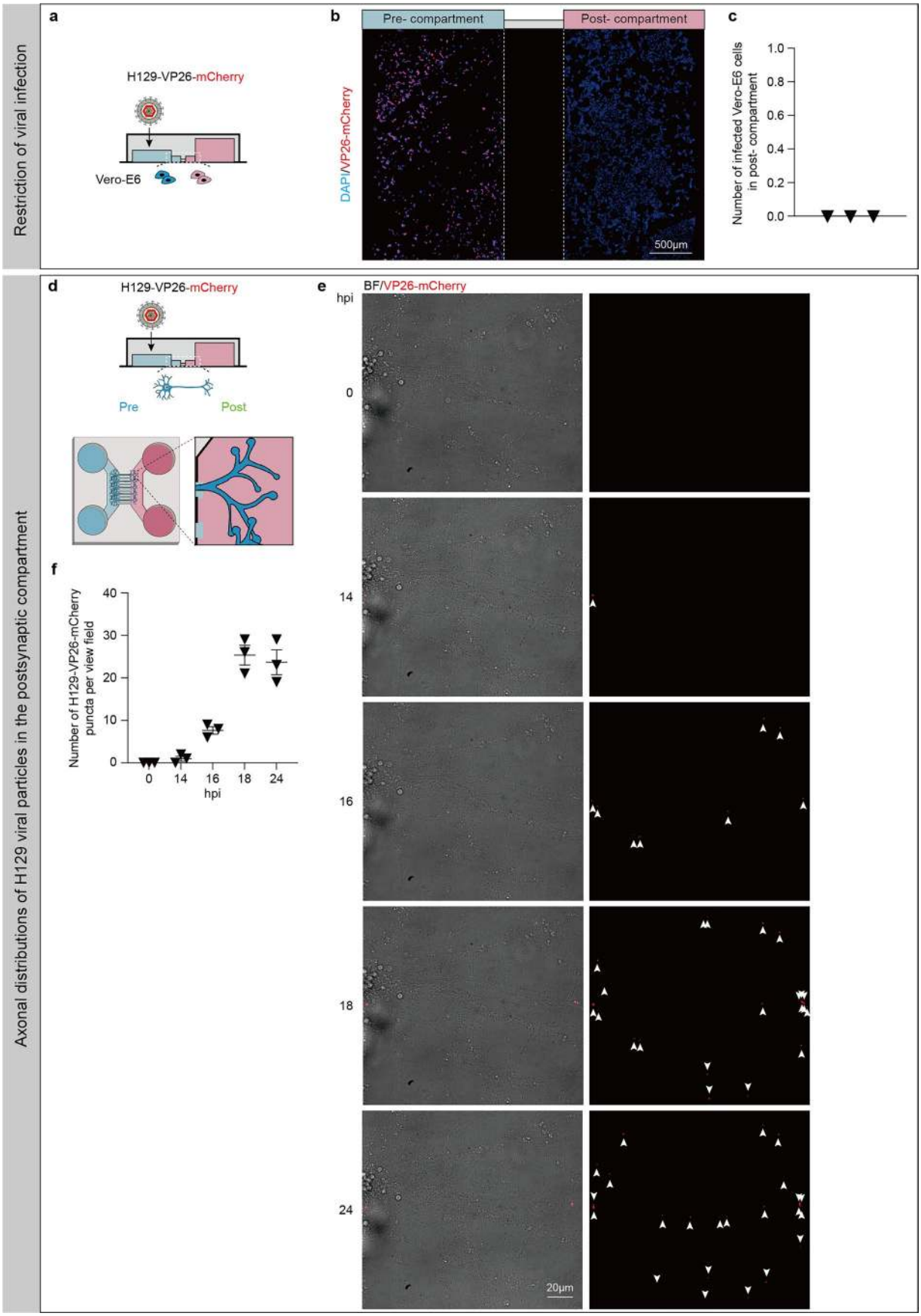

Extended Data Fig. 2 | See next page for caption.

https://doi.org/10.1038/s41593-026-02254-8

Extended Data Fig. 2 | H129 infection occurs only in the loading chamber under hydrostatic pressure, and more viral particles are transported to the postsynaptic compartment by axonal transportation at 16hpi. **a**–**c**, Limitation of H129 infection in the microfluidic chamber. **a**, Diagram of leakage test of the microfluidic chamber. Vero-E6 cells were cultured on both sides of the microfluidic chamber, and 1×10^6 PFU of H129-VP26-mCherry was added into the precompartment with negative hydrostatic pressure. At 24hpi, samples were collected for analysis. **b**, Confocal image of infected Vero-E6 cells in the pre- and postcompartments. Dashed lines indicate the borders of microgrooves. **c**, Quantification of infected Vero-E6 cells in the postcompartment. **d**–**f**, Axonal distribution of H129 particles in the postcompartment at the indicated times. **d**, Diagram of neuron culture and viral infection. Neurons were cultured in the precompartment for 21 days and then infected with H129-VP26-mCherry at an MOI of 1. The axonal distribution of H129 particles in the postcompartment near the microgrooves was monitored by live imaging during infection. **e**, Representative confocal images show axonal distribution of H129 particles in the postcompartment at the indicated times (brightfield, BF; VP26-mCherry, red). **f**, Quantification of H129 particles per view field. Data are represented as mean ± s.e.m.

https://doi.org/10.1038/s41593-026-02254-8

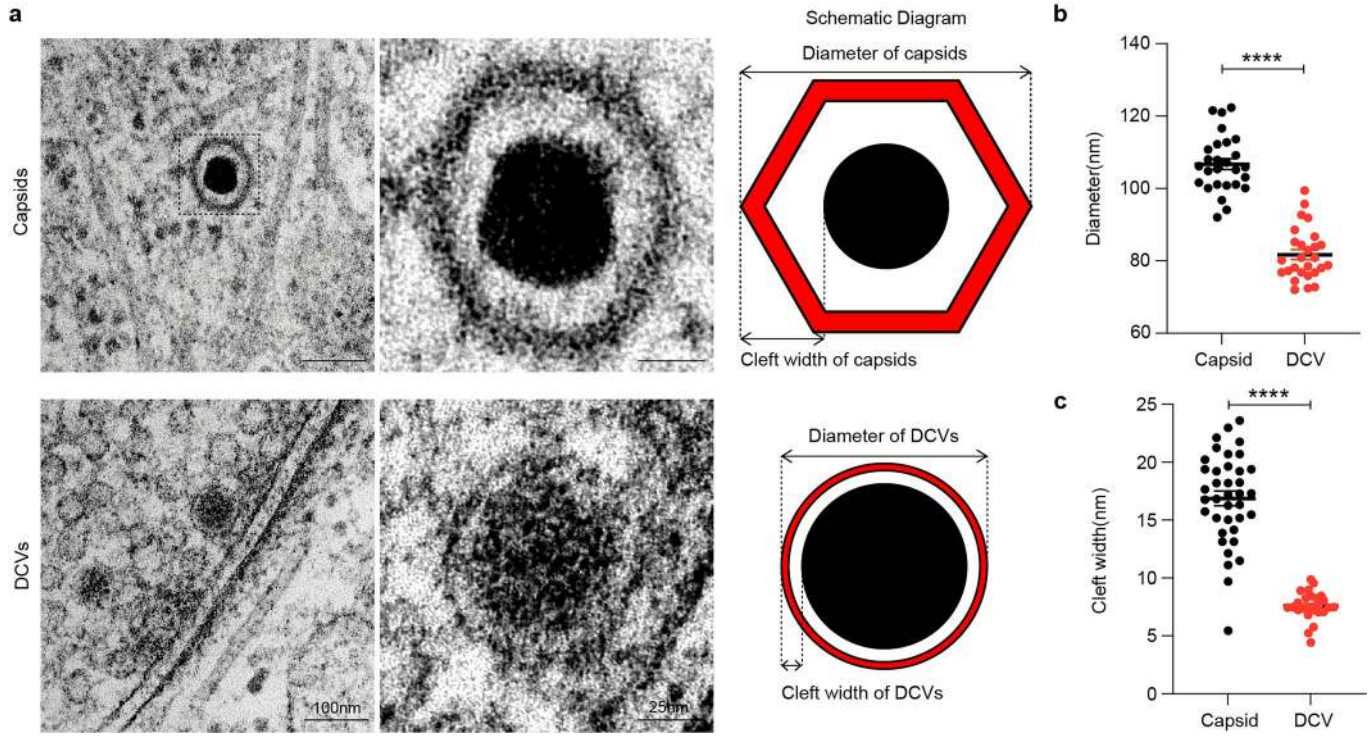

Extended Data Fig. 3 | Distinguishes H129 capsid from dense cored vesicle (DCV) by diameter and cleft width. a, TEM images of H129 capsid and DCV and their corresponding schematic diagram. The content in H129 capsid is DNA, which is highly condensed and electron-dense; while in the DCV is mostly proteins/peptides, and electron-density is lower, thus morphology is different. More distinct, diameter and cleft width are different and further introduced for analysis. **b**,**c**, Diameter (**b**) and cleft width (**c**) differences between H129 capsids and DCVs. Data were analyzed by two-tailed unpaired t test, and results are represented as mean ± s.e.m. ****$p < 0.0001$.

https://doi.org/10.1038/s41593-026-02254-8

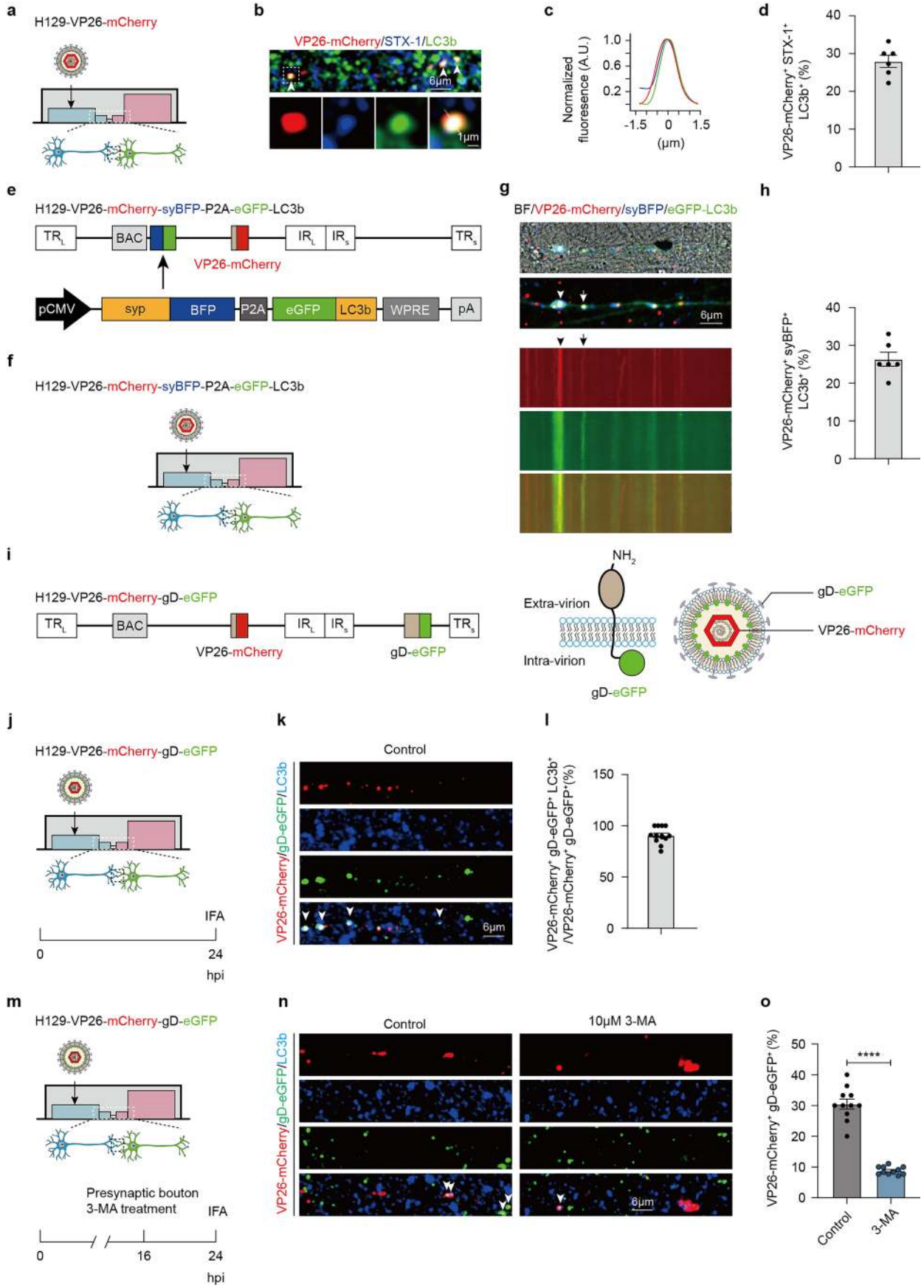

Extended Data Fig. 4 | See next page for caption.

https://doi.org/10.1038/s41593-026-02254-8

Extended Data Fig. 4 | Effect of 3-MA treatment on presynaptic assembly of H129. a–**d**, Colocalization of H129 with LC3b at presynaptic boutons by IFA. **a**, Diagram of infection presynaptic neurons with H129-VP26-mCherry. **b**, Colocalization (white arrowhead, zoomed in on the bottom) of VP26-mCherry (red), STX-1 (blue), and LC3b (green) (top panel). **c**, Normalized line profiles of VP26-mCherry, STX-1, and LC3b intensity, respectively. **d**, Colocalization rate of VP26-mCherry with both STX-1 and LC3b. **e**–**h**, Colocalization and cotransportation of H129 particles with LC3b at presynaptic boutons by live imaging. **e**,**f**, Schematic diagram of H129-VP26-mCherry-syBFP-P2A-eGFP-LC3b (**e**) and infection of presynaptic neurons (**f**). **g**, Live images show colocalization (arrowhead)/cotransportation (arrow) of VP26-mCherry and eGFP-LC3b at presynaptic boutons. Brightfield (BF), VP26-mCherry (red), syBFP (blue), and eGFP-LC3b (green) are shown (top two panels). The corresponding kymographs are shown (bottom three panels). **h**, Colocalization rate of VP26-mCherry with syBFP and eGFP-LC3b. **i**–**l**, Colocalization analysis of VP26-mCherry, gD-eGFP and LC3b. **i**, Genetic and structural diagram of H129-VP26-mCherry-gD-eGFP. **j**, Diagram of H129-VP26-mCherry-gD-eGFP infection. **k**, Colocalization (white arrowhead) of VP26-mCherry (red), gD-eGFP (green) and LC3b (blue). **l**, Quantification of the proportion of $LC3b^+$ enveloped viral particles ($VP26\text{-}mCherry^+$ $gD\text{-}eGFP^+$ $LC3b^+$/$VP26\text{-}mCherry^+$ $gD\text{-}eGFP^+$ ·100%). **m**–**o**, Effect of 3-MA treatment on H129 assembly. **m**, DIV21 presynaptic neurons were infected with H129-VP26-mCherry-gD-eGFP (MOI = 1), and 10 μM 3-MA was added to the postsynaptic compartment (including terminals of presynaptic neurons and postsynaptic neurons) at 16hpi. Neurons were fixed for IFA analysis at 24hpi. **n**, Colocalization (white arrowhead) of VP26-mCherry and gD-eGFP. **o**, Quantification of the colocalization of VP26-mCherry and gD-eGFP after treatment with 3-MA treatment. Data were analyzed by two-tailed unpaired t-test. Data are represented as mean ± s.e.m. ****$p < 0.0001$.

https://doi.org/10.1038/s41593-026-02254-8

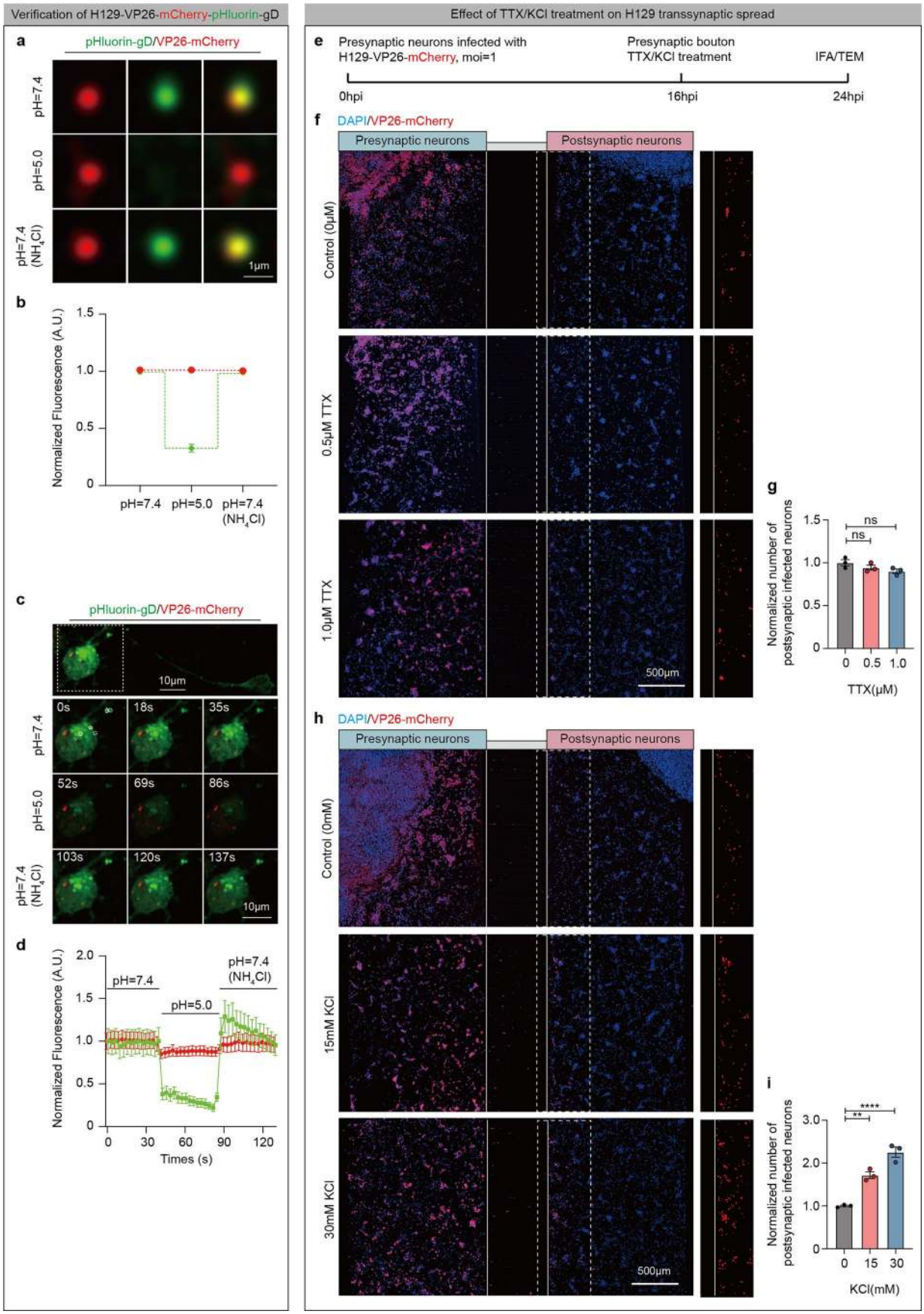

Extended Data Fig. 5 | See next page for caption.

https://doi.org/10.1038/s41593-026-02254-8

Extended Data Fig. 5 | KCl facilitates H129 spread from presynaptic neuron to postsynaptic neuron, but TTX has no effect. a,**b**, Fluorescence of H129-VP26-mCherry-pHluorin-gD viral particle at different pH conditions. **a**, Confocal images show H129-VP26-mCherry-pHluorin-gD viral particles in Tyrode's solution (pH = 7.4), Tyrode's-MES (pH = 5.0) and Tyrode's-NH_4Cl (pH = 7.4). **b**, Normalized fluorescence of pHluorin-gD and VP26-mCherry in different solutions. Data are represented as mean ± s.e.m. **c**, Fluorescence in H129-VP26-mCherry-pHluorin-gD infected neurons perfused with different pH solutions. pHluorin-gD (green) and VP26-mCherry (red) are shown (top panel); the dashed-line circle indicates the ROI exposed to different buffers for analysis (bottom panels). **d**, Normalized fluorescence traces of pHluorin-gD and VP26-mCherry in different buffers. **e**, Timeline of virus infection and TTX or KCl treatment. DIV21 presynaptic neurons were infected with H129-VP26-mCherry (MOI = 1), and TTX and KCl were separately added to the presynaptic boutons at 16hpi. At 24hpi, neurons were fixed for IFA and TEM analysis. **f**,**g**, The effect of TTX on H129 spread. **f**, Confocal images show H129-VP26-mCherry transneuronal spread after TTX treatment from 16hpi to 24hpi. Solid line marks microgroove borders; dashed rectangle (right panel) shows VP26-mCherry signal only. **g**, Normalized number of postsynaptic infected neurons after TTX treatment. Data were analyzed by one-way ANOVA, Tukey test. **h**,**i**, The effect of KCl on H129 spread. **h**, Confocal images show H129-VP26-mCherry transneuronal spread with KCl treatment for 5 min and analyzed at 24hpi. Solid line marks microgroove borders; dashed rectangle (right panel) shows VP26-mCherry signal only. **i**, Normalized number of postsynaptic infected neurons after KCl treatment. Data were analyzed by one-way ANOVA, Tukey test. Data are represented as mean ± s.e.m. ns: no significant, $^{**}p < 0.01$ and $^{****}p < 0.0001$.

https://doi.org/10.1038/s41593-026-02254-8

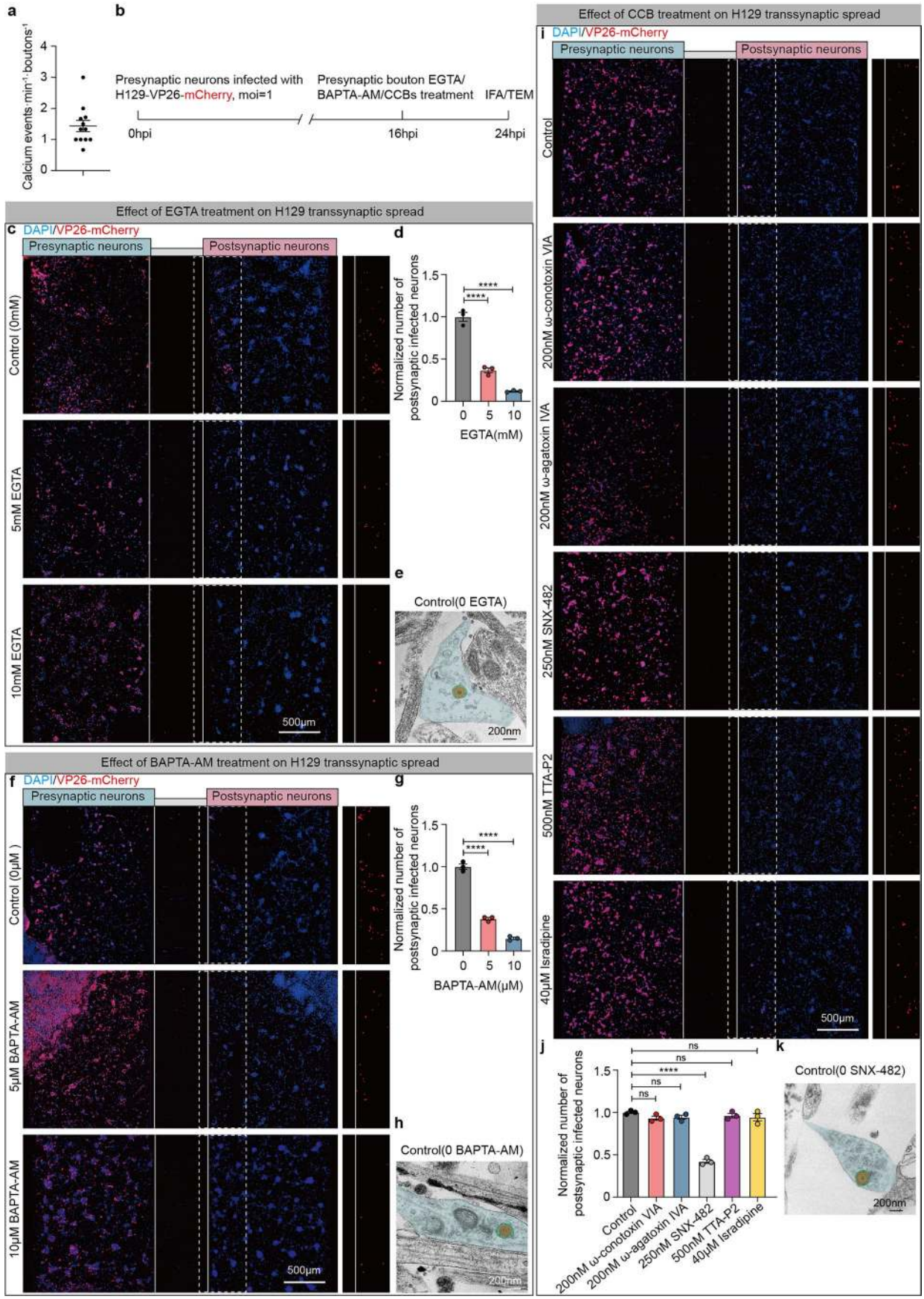

Extended Data Fig. 6 | See next page for caption.

https://doi.org/10.1038/s41593-026-02254-8

Extended Data Fig. 6 | Ca^{2+} influx via R-type channel is essential for H129 spread from presynaptic neuron to postsynaptic neuron. a, Frequency of calcium events after H129 infection (calcium events min^{-1} $boutons^{-1}$). **b**, Timeline of virus infection and EGTA/BAPTA-AM/calcium channel blockers (CCBs) treatment. **c**,**d**, Effect of EGTA on H129 spread. **c**, Confocal images show H129-VP26-mCherry transneuronal spread after EGTA treatment. Solid line marks microgroove borders; dashed rectangle (right panel) shows VP26-mCherry signal only. **d**, Normalized number of postsynaptic infected neurons after EGTA treatment. Data were analyzed by one-way ANOVA, Tukey test. **e**, TEM image of H129 particle in presynaptic boutons without EGTA treatment. Pseudocolor of light red merged with green indicated 'virion vesicle'. **f**,**g**, Effect of BAPTA-AM on H129 spread, similar to **c** and **d**. Data were analyzed by one-way ANOVA, Tukey test. **h**, TEM image of H129 particle in presynaptic boutons without BAPTA-AM treatment. Pseudocolor of light red merged with green indicates 'virion vesicle'. **i**,**j**, Effect of CCBs on H129 spread, similar to **c** and **d**. Data were analyzed by one-way ANOVA, Tukey test. **k**, TEM image of H129 viral particle in presynaptic boutons without SNX-482 treatment. Pseudocolor of light red merged with green indicates 'virion vesicle'. Data are represented as mean ± s.e.m. ns: no significant and ****$p < 0.0001$.

https://doi.org/10.1038/s41593-026-02254-8

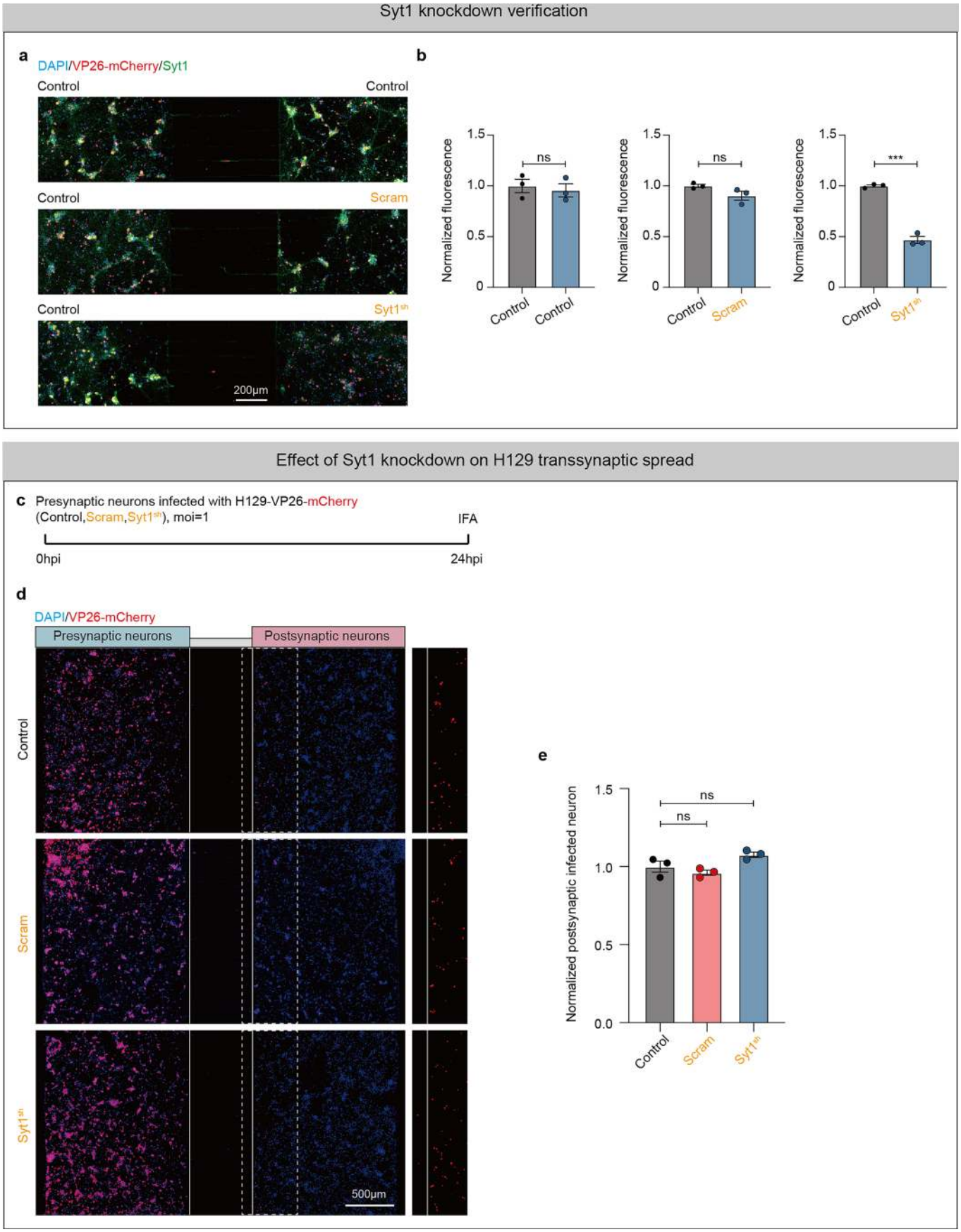

Extended Data Fig. 7 | See next page for caption.

https://doi.org/10.1038/s41593-026-02254-8

Extended Data Fig. 7 | Synaptotagmin-1 (Syt1) knockdown does not significantly influence H129 spread from presynaptic neuron to postsynaptic neuron. a,**b**, Syt1 knockdown with H129-VP26-mCherry-Syt1^{sh}. **a**, Confocal images show Syt1 knockdown efficiency by H129-VP26-mCherry-Syt1^{sh}. Presynaptic neurons were all infected with H129-VP26-mCherry (control). Meanwhile, postsynaptic neurons were infected with controls of H129-VP26-mCherry (control) and H129-VP26-mCherry-Scram (scram), or H129-VP26-mCherry-Syt1^{sh} (Syt1^{sh}), respectively. **b**, Samples were collected at 16hpi for normalized Syt1 fluorescence intensity analysis. Data were analyzed by two-tailed unpaired t test. **c**–**e**, Effect of Syt1 knockdown on H129 spread. **c**, DIV21 presynaptic neurons were infected with control, scram, and Syt1^{sh} (MOI = 1). At 24hpi, neurons were fixed for IFA analysis. **d**, Confocal images show transneuronal spread of control, scram, and Syt1^{sh}. Solid line marks microgroove borders; dashed rectangle (right panel) shows VP26-mCherry signal only. **e**, Normalized number of postsynaptic infected neurons after presynaptic neurons infected with control, scram, and Syt1^{sh}. Data were analyzed by one-way ANOVA, Tukey test. Data are represented as mean ± s.e.m. ns: no significant and ***$p < 0.001$.

https://doi.org/10.1038/s41593-026-02254-8

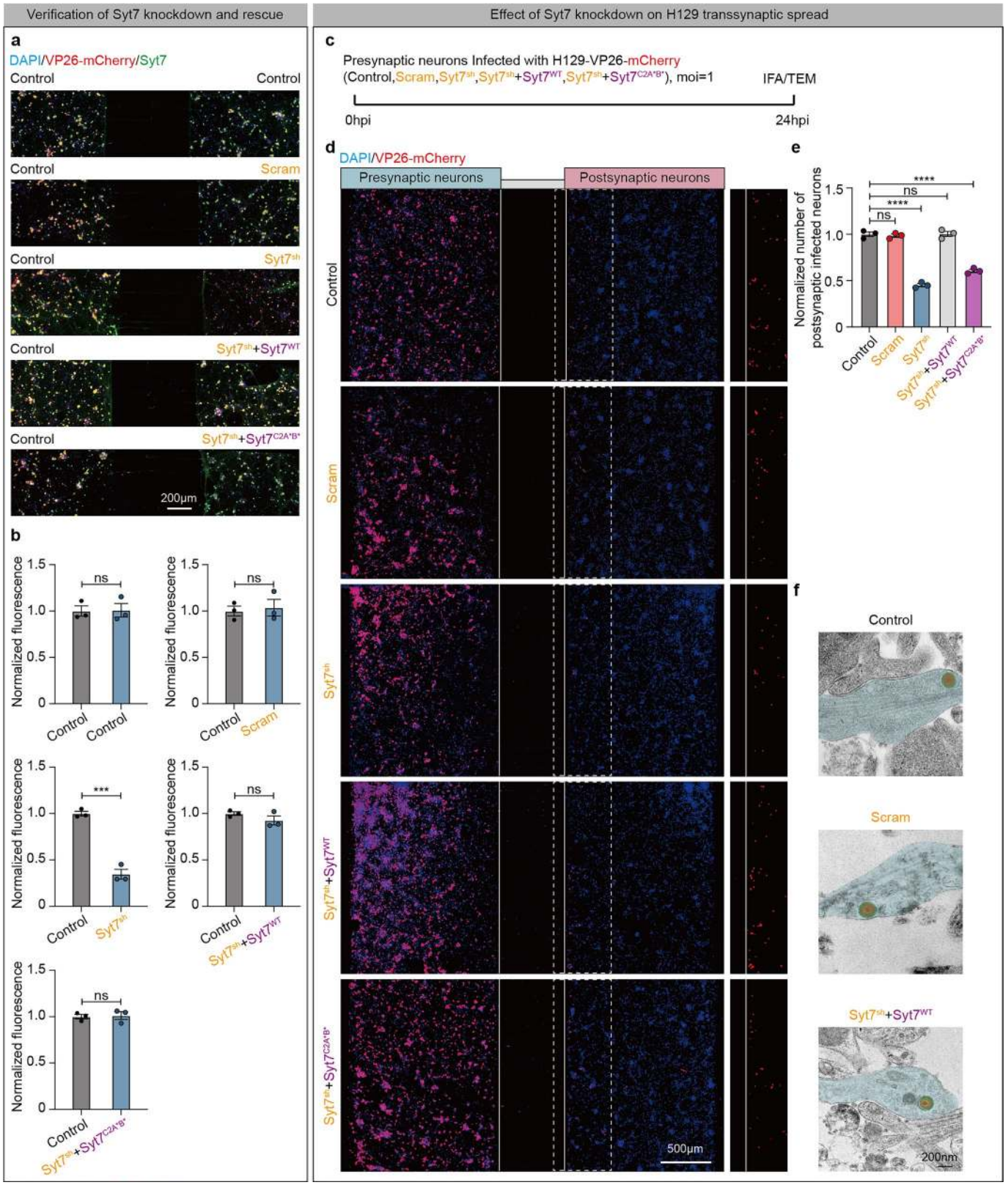

Extended Data Fig. 8 | See next page for caption.

https://doi.org/10.1038/s41593-026-02254-8

Extended Data Fig. 8 | The calcium-binding domain of Syt7 is required for H129 spread from the presynaptic neuron to the postsynaptic neuron.
a, Confocal images show Syt7 knockdown and rescue by H129-VP26-mCherry-Syt7^{sh} (Syt7^{sh}), H129-VP26-mCherry-Syt7^{sh} + Syt7^{WT} (Syt7^{sh} + Syt7^{WT}) and H129-VP26-mCherry-Syt7^{sh} + Syt7^{C2A*B*} (Syt7^{sh} + Syt7^{C2A*B*}). All the presynaptic neurons were infected with H129-VP26-mCherry (control). Meanwhile, postsynaptic neurons were infected with control, scram, Syt7^{sh}, Syt7^{sh} + Syt7^{WT}, and Syt7^{sh} + Syt7^{C2A*B*}, respectively. Samples were collected at 16hpi for Syt7 fluorescence intensity analysis in postsynaptic neurons. **b**, Normalized Syt7 fluorescence intensity analysis. Data were analyzed by two-tailed unpaired t test. **c**–**e**, Calcium-binding domain of Syt7 and H129 spread. **c**, Timeline of virus infection. DIV21 presynaptic neurons were infected with controls of H129-VP26-mCherry (control) and H129-VP26-mCherry-Scram (scram), H129-VP26-mCherry-Syt7^{sh} (Syt7^{sh}), H129-VP26-mCherry-Syt7^{sh} + Syt7^{WT} (Syt7^{sh} + Syt7^{WT}), and H129-VP26-mCherry-Syt7^{sh} + Syt7^{C2A*B*} (Syt7^{sh} + Syt7^{C2A*B*}) (MOI = 1), respectively. Neurons were fixed for IFA and TEM analysis at 24hpi. **d**, Confocal images show transneuronal spread of control, scram, Syt7^{sh}, Syt7^{sh} + Syt7^{WT}, and Syt7^{sh} + Syt7^{C2A*B*}. Solid line marks microgroove borders; dashed rectangle (right panel) shows VP26-mCherry signal only. **e**, Normalized number of postsynaptic infected neurons after Syt7 knockdown, rescue, and calcium binding domain mutation. Data were analyzed by one-way ANOVA, Tukey test. **f**, TEM image of H129 particle in presynaptic bouton after infection of control, scram, and Syt7^{sh} + Syt7^{WT}. Pseudocolor of light red merged with green indicates 'virion vesicle'. Data are represented as mean ± s.e.m., ns: no significant, ***$p < 0.001$ and ****$p < 0.0001$.

https://doi.org/10.1038/s41593-026-02254-8

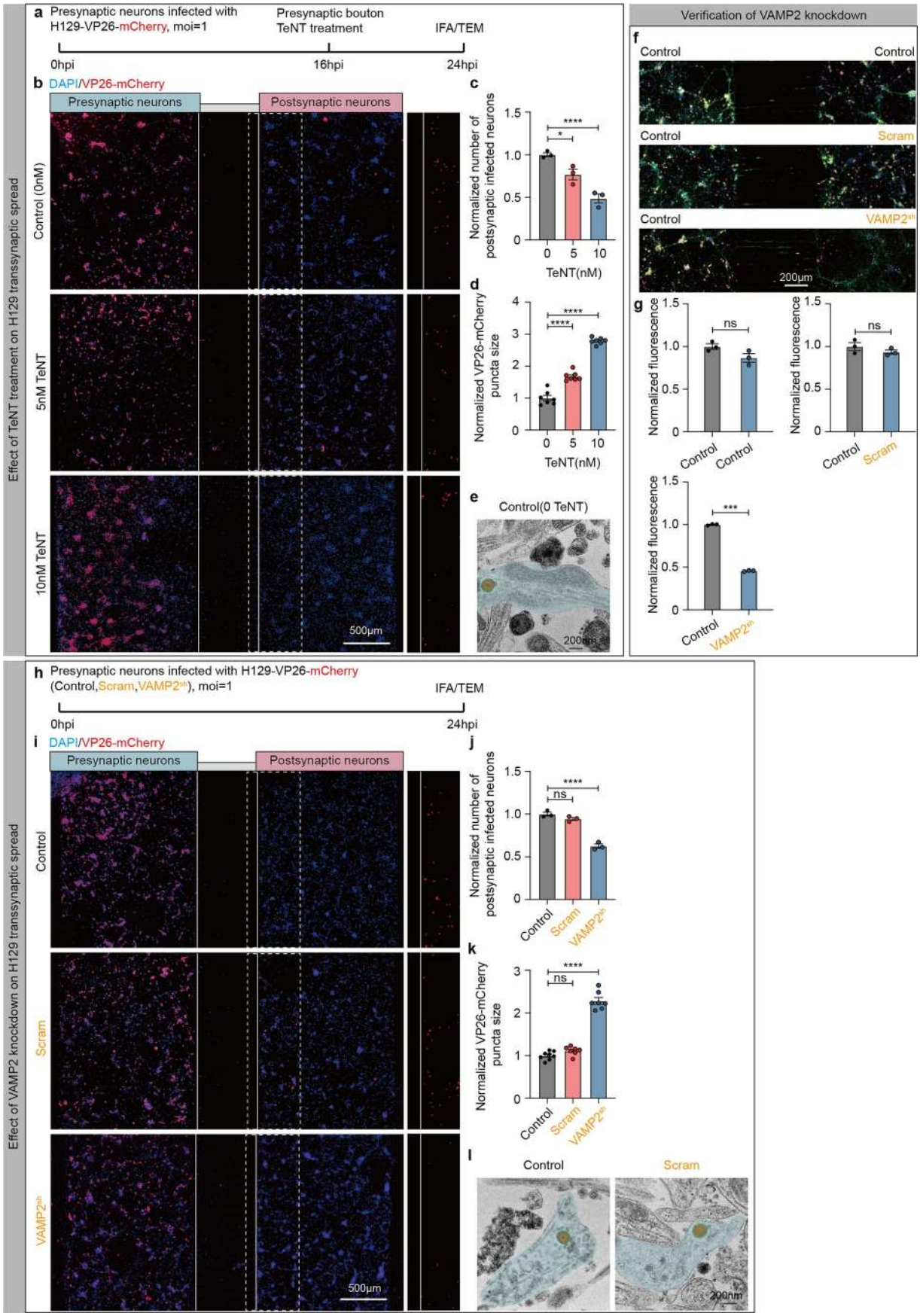

Extended Data Fig. 9 | See next page for caption.

https://doi.org/10.1038/s41593-026-02254-8

Extended Data Fig. 9 | VAMP2 is important for H129 spread from presynaptic neuron to postsynaptic neuron. a–**c**, Effect of TeNT on H129 spread. **a**, Timeline of virus infection and TeNT treatment. **b**, Confocal images show H129-VP26-mCherry transneuronal spread after TeNT treatment. Solid line marks microgroove borders; dashed rectangle (right panel) shows VP26-mCherry signal only. **c**, Normalized number of postsynaptic infected neurons after TeNT treatment. Data were analyzed by one-way ANOVA, Tukey test. **d**, Normalized VP26-mCherry puncta size at presynaptic boutons after TeNT treatment. Data were analyzed by one-way ANOVA, Tukey test. **e**, TEM image of H129 viral particle in presynaptic boutons (control, 0 TeNT). Pseudocolor of light red merged with green indicates 'virion vesicle'. **f**,**g**, VAMP2 knockdown efficiency. **f**, Confocal images show VAMP2 knockdown efficiency by H129-VP26-mCherry-VAMP2^{sh}. All the presynaptic neurons were infected with H129-VP26-mCherry (control). Meanwhile, postsynaptic neurons were infected with H129-VP26-mCherry (control) and H129-VP26-mCherry-Scram (scram), and H129-VP26-mCherry-VAMP2^{sh} (VAMP2^{sh}), respectively. Samples were collected at 16hpi for VAMP2 intensity analysis by IFA. **g**, Normalized VAMP2 fluorescence intensity analysis after being infected with the viruses. Data were analyzed by two-tailed unpaired t test. **h**–**j**, Effect of VAMP2 knockdown on H129 spread, similar to **a**–**c**. Data were analyzed by one-way ANOVA, Tukey test. **k**, Normalized VP26-mCherry puncta size at presynaptic boutons after VAMP2 knockdown. Data were analyzed by one-way ANOVA, Tukey test. **l**, TEM image of H129 particle in presynaptic boutons after infection of control and scram. Pseudocolor of light red merged with green indicates 'virion vesicle'. Data are represented as mean ± s.e.m. ns: no significant, *$p < 0.05$, ***$p < 0.001$ and ****$p < 0.0001$.

https://doi.org/10.1038/s41593-026-02254-8

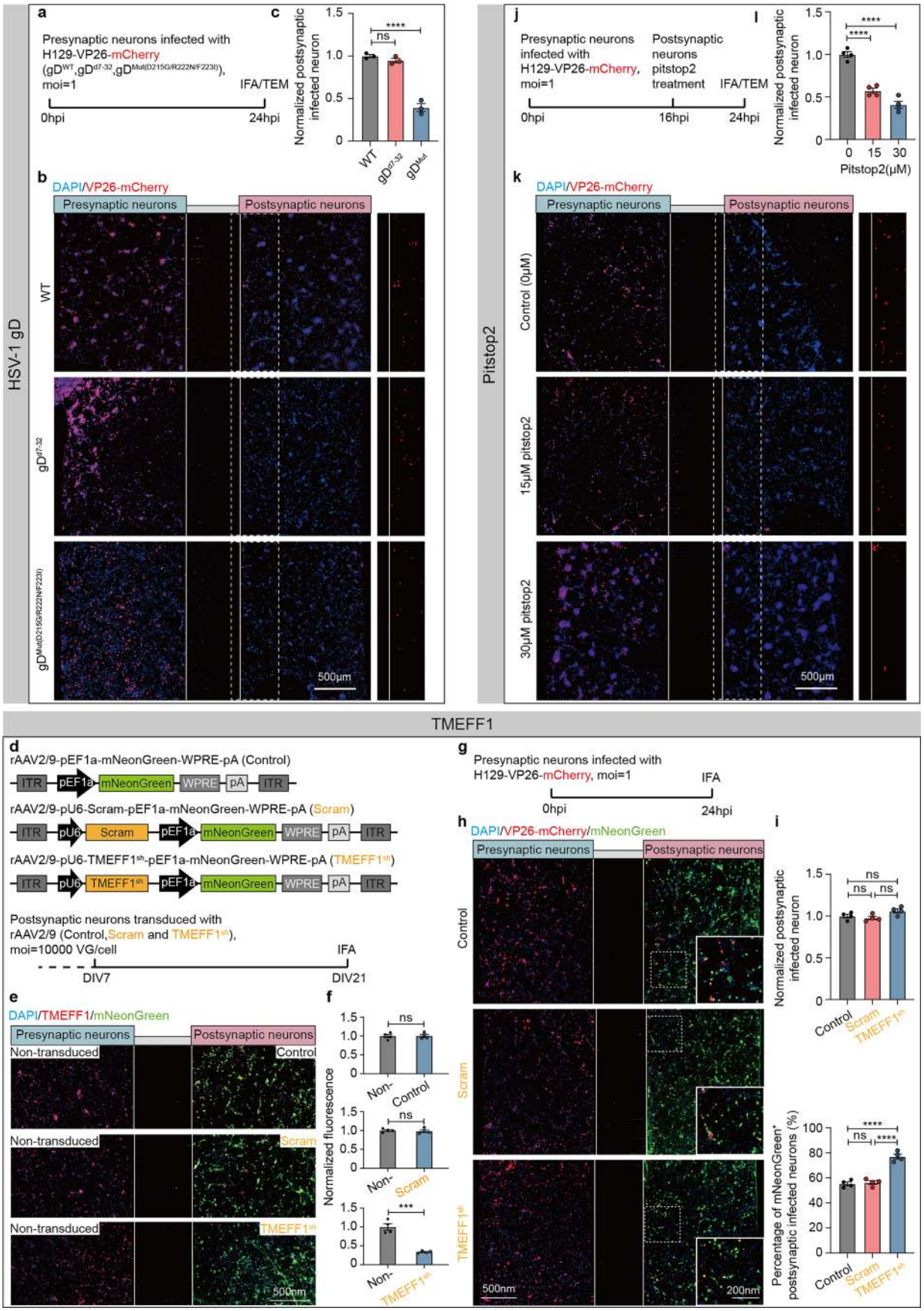

Extended Data Fig. 10 | See next page for caption.

https://doi.org/10.1038/s41593-026-02254-8

Extended Data Fig. 10 | Interaction of gD and nectin-1, and clathrin-mediated endocytosis are necessary for H129 spread from presynaptic neuron to postsynaptic neuron. a–**c**, H129-gD mutants and H129 spread. **a**, Timeline of virus infection. **b**, Confocal images show transneuronal spread of H129-VP26-mCherry (gD^{WT}), gD mutants of H129-VP26-mCherry-$gD^{d7\text{-}32}$ ($gD^{d7\text{-}32}$) and H129-VP26-mCherry-$gD^{Mut\ (D215G/R222N/F223I)}$ ($gD^{Mut\ (D215G/R222N/F223I)}$). Solid line marks microgroove borders; dashed rectangle (right panel) shows VP26-mCherry signal only. **c**, Normalized number of postsynaptic infected neurons after infected with gD^{WT}, $gD^{d7\text{-}32}$ and $gD^{Mut\ (D215G/R222N/F223I)}$. Data were analyzed by one-way ANOVA, Tukey test. **d**–**i**, TMEFF1 and H129 postsynaptic entry. **d**, Schematic genome diagrams and workflow of the transduction of three rAAV2/9 knockdown vectors. rAAV2/9-pEF1a-mNeonGreen-WPRE-pA (control), rAAV2/9-pU6-scram-pEF1a-mNeonGreen-WPRE-pA (scram), and rAAV2/9-pU6-$TMEFF1^{sh}$-pEF1a-mNeonGreen-WPRE-pA ($TMEFF1^{sh}$). **e**, Confocal images show TMEFF1 knockdown efficiency by the rAAV2/9 vectors. The solid line marks microgroove borders. **f**, Normalized TMEFF1 fluorescence intensity analysis. Data were analyzed by two-tailed unpaired t test. **g**, Workflow of H129-VP26-mCherry infection. **h**, Confocal images show transsynaptic spread of H129-VP26-mCherry after postsynaptic neurons transduced with control, scram, or $TMEFF1^{sh}$ vectors. The solid line marks microgroove borders; the boxed areas are zoomed in on the bottom-right. **i**, Quantification of the normalized number of postsynaptic infected neurons (top panel) and percentage of $mNeonGreen^{+}$ postsynaptic infected neurons (bottom panel). Data were analyzed by one-way ANOVA, Tukey test. **j**,**k**, Pitstop2 treatment and H129 spread. **j**, Timeline of virus infection and Pitstop2 treatment. **k**, Confocal images show H129-VP26-mCherry transneuronal spread after Pitstop2 treatment. Solid line marks microgroove borders; dashed rectangle (right panel) shows VP26-mCherry signal only. **l**, Normalized number of postsynaptic infected neurons after Pitstop2 treatment. Data were analyzed by one-way ANOVA, Tukey test. Data are represented as mean ± s.e.m. ns: not significant and ***$p < 0.001$ and ****$p < 0.0001$.

nature portfolio

Corresponding author(s): Min-Hua Luo

Last updated by author(s): Feb 27, 2026

Reporting Summary

Nature Portfolio wishes to improve the reproducibility of the work that we publish. This form provides structure for consistency and transparency in reporting. For further information on Nature Portfolio policies, see our Editorial Policies and the Editorial Policy Checklist.

Statistics

For all statistical analyses, confirm that the following items are present in the figure legend, table legend, main text, or Methods section.

n/a	Confirmed	
☐	☒	The exact sample size (*n*) for each experimental group/condition, given as a discrete number and unit of measurement
☐	☒	A statement on whether measurements were taken from distinct samples or whether the same sample was measured repeatedly
☐	☒	The statistical test(s) used AND whether they are one- or two-sided *Only common tests should be described solely by name; describe more complex techniques in the Methods section.*
☐	☒	A description of all covariates tested
☐	☒	A description of any assumptions or corrections, such as tests of normality and adjustment for multiple comparisons
☐	☒	A full description of the statistical parameters including central tendency (e.g. means) or other basic estimates (e.g. regression coefficient) AND variation (e.g. standard deviation) or associated estimates of uncertainty (e.g. confidence intervals)
☐	☒	For null hypothesis testing, the test statistic (e.g. *F*, *t*, *r*) with confidence intervals, effect sizes, degrees of freedom and *P* value noted *Give P values as exact values whenever suitable.*
☒	☐	For Bayesian analysis, information on the choice of priors and Markov chain Monte Carlo settings
☒	☐	For hierarchical and complex designs, identification of the appropriate level for tests and full reporting of outcomes
☒	☐	Estimates of effect sizes (e.g. Cohen's *d*, Pearson's *r*), indicating how they were calculated

Our web collection on statistics for biologists contains articles on many of the points above.

Software and code

Policy information about availability of computer code

Data collection	Immunofluorescent images and live-imaging data were acquired using Andor Dragonfly 202 equipped with a Leica 60×/1.40 oil objective. Electron micrographs were acquired on FEI Tecnai G2 20 TWIN transmission electron microscope.
Data analysis	Immunofluorescent images and live-imaging data were analysis by ImageJ (version: 2.9.0). Image J plugins of 'Bleach Correction' and 'StackReg' were used for live-imaging analysis. GraphPad Prism (version: 9.4.1) was used to perform statistical analyses. The distributions of pore membrane angle and depth of the secretion cavity were analyzed by Origin Pro 2019b (version: 9.6.5). No custom-programed code or software was used in this study.

For manuscripts utilizing custom algorithms or software that are central to the research but not yet described in published literature, software must be made available to editors and reviewers. We strongly encourage code deposition in a community repository (e.g. GitHub). See the Nature Portfolio guidelines for submitting code & software for further information.

Data

Policy information about availability of data

All manuscripts must include a data availability statement. This statement should provide the following information, where applicable:

- Accession codes, unique identifiers, or web links for publicly available datasets
- A description of any restrictions on data availability
- For clinical datasets or third party data, please ensure that the statement adheres to our policy

Data underlying all Figures and Extended Data Figures are provided with the paper. Source data are provided with this paper.

Research involving human participants, their data, or biological material

Policy information about studies with human participants or human data. See also policy information about sex, gender (identity/presentation), and sexual orientation and race, ethnicity and racism.

Reporting on sex and gender	N/A
Reporting on race, ethnicity, or other socially relevant groupings	N/A
Population characteristics	N/A
Recruitment	N/A
Ethics oversight	N/A

Note that full information on the approval of the study protocol must also be provided in the manuscript.

Field-specific reporting

Please select the one below that is the best fit for your research. If you are not sure, read the appropriate sections before making your selection.

☒ Life sciences ☐ Behavioural & social sciences ☐ Ecological, evolutionary & environmental sciences

For a reference copy of the document with all sections, see nature.com/documents/nr-reporting-summary-flat.pdf

Life sciences study design

All studies must disclose on these points even when the disclosure is negative.

Sample size	Sample size was based on estimation from previous studies, including our own published studies. (Lo, L., et al. Neuron, 2011 and Zeng, W. B. et al. Mol Neurodegener 2017, Yang, H., et al. Mol Neurodegener 2022)
Data exclusions	No data were excluded.
Replication	For colocalization analysis, all IFA data were collected from at least four independent experiments using four different batches of primary neurons cultured in microfluidic chambers. Each independent experiment was performed in technical triplicate using the same batch of cultured neurons, and at least three fields of view per technical replicate were analyzed. For the TEM analysis (including pie charts and bar graphs), results were pooled from three independent experiments using three separate batches of cultured neurons. Each biological replicate included three technical repeats, and at least two sample positions near the postsynaptic microgrooves were processed for in situ slicing in each technical repeat. From each position, a minimum of three ultrathin sections were prepared, and dozens of fields of view per slice were imaged and analyzed.
Randomization	Data collection was randomized.
Blinding	Data collection and analysis were not performed blind to the conditions of the experiments.

Reporting for specific materials, systems and methods

We require information from authors about some types of materials, experimental systems and methods used in many studies. Here, indicate whether each material, system or method listed is relevant to your study. If you are not sure if a list item applies to your research, read the appropriate section before selecting a response.

Materials & experimental systems

n/a	Involved in the study
☐	☒ Antibodies
☐	☒ Eukaryotic cell lines
☒	☐ Palaeontology and archaeology
☐	☒ Animals and other organisms
☒	☐ Clinical data
☒	☐ Dual use research of concern
☒	☐ Plants

Methods

n/a	Involved in the study
☒	☐ ChIP-seq
☒	☐ Flow cytometry
☒	☐ MRI-based neuroimaging

Antibodies

Antibodies used

synaptobrevin-2 (VAMP2, 1:1000, IgG1, 104 211, synaptic system),
syntaxin-1(1:500, IgG1, 110 011, synaptic system),
PSD95 (1:500, IgG2a, 75-028, NeuroMab),
synaptotagmins-1 (1:200, IgG2a, 105011, synaptic system),
synaptotagmins-7 (1:500, rabbit polyclonal, 105173, synaptic system),
LC3b (1:500, rabbit polyclonal, 4108, Cell signaling technology),
TMEFF1 (1:100, mouse monoclonal IgG2b, sc-393457, Santa Cruz)
nectin-1 (1:500, rabbit polyclonal, ab229464, abcom),
CHC1 (1:500, rabbit polyclonal, ab21679, abcom),
Goat anti-Mouse IgG2a Cross-Adsorbed Secondary Antibody, Alexa Fluor™ 488 (A-21131,Thermofisher Scientific),
Goat anti-Mouse IgG1 Cross-Adsorbed Secondary Antibody, Alexa Fluor™ 647 (A-21240, Thermofisher Scientific),
Goat anti-Rabbit IgG (H+L) Highly Cross-Adsorbed Secondary Antibody, Alexa Fluor™ 647 (A-21245, Thermofisher Scientific).

Validation

synaptobrevin-2(VAMP2): K.O. validation,
syntaxin-1: validation by manufacturer by WB, IP, ICC, IHC...
PSD95: K.O. validation,
synaptotagmins-1: K.O. validation,
synaptotagmins-7: K.O. validation,
LC3b: validation by manufacturer by WB and ICC,
TMEFF1: validation by manufacturer by WB, IP, ICC and ELISA,
nectin-1: validation by manufacturer by WB and ICC,
CHC1: validation by manufacturer by WB and ICC,
Goat anti-Mouse IgG2a Cross-Adsorbed Secondary Antibody, Alexa Fluor™ 488: validation by manufacturer,
Goat anti-Mouse IgG2b Cross-Adsorbed Secondary Antibody, Alexa Fluor™ 647: validation by manufacturer,
Goat anti-Mouse IgG1 Cross-Adsorbed Secondary Antibody, Alexa Fluor™ 647: validation by manufacturer,
Goat anti-Rabbit IgG (H+L) Highly Cross-Adsorbed Secondary Antibody, Alexa Fluor™ 647: validation by manufacturer.

Eukaryotic cell lines

Policy information about cell lines and Sex and Gender in Research

Cell line source(s)	Vero-E6 (ATCC-CRL 1586, purchased from ATCC), Vero-gD, HEK-293T (ATCC-CRL 11268, purchased from ATCC)
Authentication	ATCC.
Mycoplasma contamination	Not detected for mycoplasma contamination.
Commonly misidentified lines (See ICLAC register)	No commonly misidentified cell lines were used in the study.

Animals and other research organisms

Policy information about studies involving animals; ARRIVE guidelines recommended for reporting animal research, and Sex and Gender in Research

Laboratory animals	E16.5 C57BL/6 embryos for primary mouse cortical neuron dissociation.
Wild animals	The study did not involve wild animals.
Reporting on sex	Both sexes were randomly used in this study.
Field-collected samples	This study did not use any field-collected samples.
Ethics oversight	All experimental procedures were approved by the Institutional Review Board and Institutional Animal Welfare Committee of Wuhan Institute of Virology, Chinese Academy of Sciences (WIVA10202001).

Note that full information on the approval of the study protocol must also be provided in the manuscript.

Plants

Seed stocks	N/A
Novel plant genotypes	N/A
Authentication	N/A